Binarity Enhances the Occurrence Rate of Quiescent Radio Emission in Ultracool Dwarfs

MELODIE M. KAO [1,2] AND J. SEBASTIAN PINEDA [3]

[1] Arizona State University, School of Earth and Space Exploration, 550 E Tyler Mall PSF 686, Tempe, AZ 85287
[2] NASA Hubble Postdoctoral Fellow
[3] University of Colorado Boulder, Laboratory for Atmospheric and Space Physics, 3665 Discovery Drive, Boulder CO, 80303, USA

ABSTRACT

We present new radio detections at 4–8 GHz of the three ultracool dwarf binary systems, GJ 564 BC, LP 415-20, and 2MASS J21402931+1625183. We modify a recently developed occurrence rate calculation framework to compare the quiescent radio occurrence rate of binary systems to single objects. We combine our new observations with data available in the literature to create samples of 179 single ultracool dwarfs (82 M dwarfs, 75 L dwarfs, and 23 T/Y dwarfs) and 28 binary ultracool dwarf systems. Using these samples, we show that binarity enhances the ultracool dwarf quiescent radio occurrence rate relative to their single counterparts.

Keywords: brown dwarfs — planets and satellites: magnetic fields — radio continuum: stars — stars: magnetic fields

1. INTRODUCTION

Since the first discovery of radio emission (Berger et al. 2001) from ultracool dwarfs with M7 and later spectral types, GHz radio observations of such objects have revolutionized our understanding of how magnetic activity evolves over the star-planet transition regime. Surveys of X-ray emission in the lowest-mass stars showed a sharp drop-off in coronal emissions at a spectral type M9.5 (Williams et al. 2014), with chromospheric Hα emission declining continuously across the L-dwarf regime (Schmidt et al. 2015; Pineda et al. 2016). Despite these declining diagnostics of magnetic activity, radio observations demonstrated persistently strong GHz emissions across the entire ultracool dwarf regime, revealing the emergence of radio aurorae (Hallinan et al. 2015; Kao et al. 2016; Pineda et al. 2017).

The radio component of ultracool dwarf aurorae manifests as periodically flaring and highly circularly polarized coherent electron cyclotron maser emission (Hallinan et al. 2007, 2008). This emission traces the fundamental cyclotron frequency of the local magnetosphere (Treumann 2006). Detections of GHz radio aurorae confirm that ultracool dwarfs at least as late as T6.5 can host strong kiloGauss magnetic fields (Route & Wolszczan

mkao@asu.edu

2012, 2016a; Williams & Berger 2015; Kao et al. 2016, 2018; Richey-Yowell et al. accepted).

Ultracool dwarfs also exhibit nonthermal and incoherent radio emission that is quasi-steady and weakly circularly polarized (e.g., Williams et al. 2015a; Kao et al. 2016, 2018). This "quiescent" radio emission is attributed to optically thin gyrosynchrotron emission (e.g. Berger et al. 2005; Osten et al. 2006; Williams et al. 2015b; Lynch et al. 2016) and can persist for years (e.g. Berger et al. 2008a; Kao et al. 2016, 2018). Furthermore, quiescent radio luminosities correlate with Hα luminosities in aurorae-emitting ultracool dwarfs, suggesting that the physical conditions underpinning ultracool dwarf radio aurorae may also be related to their quiescent radio emission (Pineda et al. 2017). Kao et al. (2019) argue that one plausible explanation are radiation belts analogous to the extended circum-planetary regions of high-energy electrons trapped in the magnetospheres of solar system planets (Sault et al. 1997; Bolton et al. 2004; Clarke et al. 2004; Horne et al. 2008). While the source of this magnetospheric plasma is unknown, possibilities include flares (e.g. Gizis et al. 2013; Paudel et al. 2018a; Jackman et al. 2019; Paudel et al. 2020) or volcanic activity from planets (Kao et al. 2018, 2019).

Recently, Kao & Shkolnik (submitted) argued for quantifying ultracool dwarf magnetic activity using their quiescent rather than periodically flaring auroral radio emission. They noted that the rarity of detected ultracool dwarf radio emission together with the wealth of

data available in the literature underscored the value of moving toward studies of radio occurrence rates as a function of object characteristics, such as $T_{\rm eff}$, mass, rotation rate, and age. Volume-limited radio surveys yield detection rates between ∼5–10% for M, L, and T ultracool dwarfs (Antonova et al. 2013; Lynch et al. 2016; Route & Wolszczan 2016b), though these studies do not separately treat binaries.

Kao & Shkolnik (submitted) developed an analytical framework for calculating occurrence rates for quiescent radio emission. By applying this framework to observations available in the literature, they show that ultracool dwarf quiescent radio occurrence rates are between $15^{+4}_{-4}\%$ – $20^{+6}_{-5}\%$ for isolated ultracool dwarfs. Furthermore, L dwarfs may have a suppressed radio occurrence rate compared to M and T/Y dwarfs.

In this work, we examine radio emission in ultracool dwarf binary systems. To date, no comprehensive study of ultracool dwarf radio emission has focused on binaries, yet such systems will provide valuable tests of ultracool dwarf magnetic activity. Unlike the field population, binaries can have precise observational constraints on individual masses and therefore ages (e.g. Konopacky et al. 2010; Dupuy & Liu 2017; Dupuy et al. 2019). Precisely known properties enable robust comparisons between individual objects and the conditions which power their radio emission. For instance, in two radio ultracool dwarf binary systems, only one component exhibits detectable GHz radio emission (Konopacky et al. 2012; Harding et al. 2013; Williams et al. 2015a; Forbrich et al. 2016). Why is one component radio bright but the other is not? Additional observations of well characterized systems, such as those presented in this work, will help elucidate this question.

Furthermore, comparing the population of single objects to ultracool dwarf binaries provides a complementary means of identifying characteristics that influence magnetic activity at the stellar-planetary boundary. For instance, in stars, tidal spin-up may enhance the rotation rates and thus the magnetic activity of the binary population (Zahn 1977; Morgan et al. 2016). No studies have examined whether similar phenomena may occur for ultracool dwarfs. Here, we assess whether binarity enhances the quiescent radio occurrence rate of ultracool dwarfs in binary systems compared to their single counterparts.

2. NEW OBSERVATIONS OF ULTRACOOL DWARF BINARY SYSTEMS

We supplement existing radio observations of ultracool dwarf binary systems with new observations of three binary systems using the *NSF's Karl G. Jansky* Very Large Array (VLA; Perley et al. 2011) from program VLA 18B-283 (PI - Pineda). Table 1 summarizes the properties of these targets and we discuss them in further detail below.

2.1. *Targets*

GJ 564 BC is also known as HD 130948BC, a benchmark brown dwarf system orbiting a solar analog (Dupuy et al. 2009). It was discovered through adaptive optics imaging at a separation of 2.64″ or ∼7.4 AU (Potter et al. 2002). It is the nearest binary in our observation sample, at ∼18 pc (*Gaia* parallax of 54.9068 ± 0.0684 mas; Gaia Collaboration 2018), and consists of two nearly equal-mass L4 dwarfs with masses of $59.8^{+2.0}_{-2.1}$ and $55.6^{+2.0}_{-1.9}$ $M_{\rm J}$ for the B and C components, respectively (Dupuy & Liu 2017). The masses and luminosities for this system constrain its age to 0.44 ± 0.04 Gyr. The binary has a semi-major axis of $2.226^{+0.014}_{-0.013}$ AU with a low eccentricity ($e = 0.1627 \pm 0.0017$) in a ∼10-year orbit (Dupuy & Liu 2017). Konopacky et al. (2012) further measured rotational velocities $v \sin i$ of 62 ± 4 km s^{-1} and 86 ± 6 km s^{-1}, for the primary and secondary, respectively. Hα emission for this system is unknown, since it is unresolved from GJ 564 A except in adaptive optics imaging.

2MASS J21402931+1625183 was first identified as a binary system by Close et al. (2002, 2003) and has a distance of ∼33 pc (*Gaia* parallax of 30.1972 ± 0.4340 mas; Gaia Collaboration 2018). Earlier attempts to determine masses for this system suggested a large primary to secondary mass ratio (∼4; Konopacky et al. 2010). Most recently, Dupuy & Liu (2017) reported that 2MASS J21402931+1625183 is an unequal-mass binary system consisting of an M8±0.5 primary with a mass of 114^{+10}_{-12} $M_{\rm J}$ and an L0.5±1.0 secondary with a mass of 69^{+8}_{-9} $M_{\rm J}$. These updated values confirm the suggestion by Konopacky et al. (2010) that their estimated mass ratio was likely too high. This low-eccentricity system ($e = 0.196 \pm 0.007$) has a semi-major axis of 4.71 ± 0.14 AU and a ∼24.4-year orbit. Dupuy & Liu (2017) did not provide an age estimate for this system, but Martin et al. (2017) reported that gravity-sensitive indices in the near-IR spectrum of this system indicate that it is not young (FLD-G classification, $\gtrsim$200 Myr) Konopacky et al. (2012) measured individual $v \sin i$ values of 13 ± 2 km s^{-1} and 37 ± 3 km s^{-1}, for the primary and secondary respectively. Furthermore, Gizis et al. (2000) did not see any Hα emission in their spectra of this target, reporting an EW of 0 Å.

LP 415-20 is the farthest system in our sample with a distance of nearly ∼40 pc (*Gaia* parallax of 25.1963 ± 0.5117 mas; Gaia Collaboration 2018). First identified as a binary by Siegler et al. (2003), it is another

Table 1. Targets

Object Name	SpT		a	π	d	$\mu_\alpha \cos\delta$	μ_δ	ref
	(Primary)	(Secondary)	(AU)	(mas)	(pc)	(mas yr^{-1})	(mas yr^{-1})	
GJ 564 BC[a]	L4 ± 1.0	L4 ± 1.0	$2.226\ ^{+0.014}_{-0.013}$	54.9068 ± 0.0684	18.2127 ± 0.0227	144.7 ± 0.8	32.4 ± 0.7	1 3 2
2MASS J21402931+1625183[b]	M8 ± 0.5	L0.5 ± 1.0	4.71 ± 0.14	30.1972 ± 0.434	33.1 ± 0.5	-77.9 ± 0.776	-85.637 ± 0.707	1 3
LP 415-20	M6 ± 1.0	M8 ± 0.5	3.73 ± 0.12	25.1963 ± 0.5117	39.6884 ± 0.8060	134.716 ± 0.912	-38.416 ± 0.619	1 3

[a] Also known as HD 130948B

References— (1) (Dupuy & Liu 2017) ; (2) (Faherty et al. 2009) ; (3) (Gaia Collaboration 2018)

Table 2. Summary of observations

Object	Obs. Date	Time on Source (hh:mm:ss)	Synthesized Beam ($'' \times ''$)	Phase Calib.	Flux Calib.
GJ 564 BC	2019 Jan 21	01:34:10	4.17 × 3.59	J1443+2501	3C286
	2019 Feb 05	01:33:59	3.15 × 2.55	J1443+2501	3C286
J2140+16	2019 Feb 03	04:15:16	4.10 × 3.65	J2139+1423	3C286
LP 415-20	2018 Dec 28	04:15:30	4.09 × 3.71	J0431+2037	3C147

NOTE—All observations were at 4–8 GHz and taken during C configuration at the VLA.

unequal-mass binary system consisting of an M6±1.0 primary with a mass of $156^{+17}_{-18}\ M_{\rm J}$ and an M8.0±0.5 secondary with a mass of $92^{+16}_{-18}\ M_{\rm J}$ (Dupuy & Liu 2017). However, Dupuy & Liu (2017) note that the mass of the primary component is much higher than expected for its luminosity and speculate that the primary may be an unresolved unequal-mass binary. If so, the primary would likely be comprised of clearly ultracool dwarf ~100 $M_{\rm J}$ and ~50 $M_{\rm J}$ components, whose combined light are estimated as an M6 object, although the spectral decomposition suggests spectra are consistent with templates of types M5-M7. This high eccentricity ($e = 0.706^{+0.011}_{-0.012}$) system has a semi-major axis of 3.73 ± 0.12 AU and a ~14.8-year orbit. The model-derived age of the secondary component is $5.0^{+1.9}_{-4.7}$ Gyr, and an unresolved binary system for the primary component points to a model-derived age of at least several hundred Myr. Using BANYAN Σ (Gagné et al. 2018), we find that LP 415-20 is a likely a member of the Hyades Cluster with ≥99% probability (750 ± 100; Brandt & Huang 2015) when using the *Gaia* parallax and proper motion data along with a mean system radial velocity of 40.8 ± 1.4 km s^{-1} (Konopacky et al. 2010). Konopacky et al. (2012) measured individual $v \sin i$ values of 40 ± 5 km s^{-1} and 37 ± 4 km s^{-1} for the primary and secondary respectively. Additionally, Miles-Páez et al. (2017) report significant photometric variability in the combined light of the system with a periodicity of ~4.36 hrs. The system also

shows Hα in emission, with an EW measurement of 4.4 Å (Gizis et al. 2000).

2.2. *Observations and Calibrations*

We summarize target observations in Table 2. For GJ 564 BC, we obtained two 2-hr observing blocks with the VLA for four total hours on sky. For 2MASS J21402931+1625183 and LP 415-20, we obtained one 5-hr observing block each.

We calibrated our measurement sets using nearby phase calibrators and the standard VLA flux calibrators 3C147 and 3C286. Typical full-bandwidth sensitivities at C configuration for 2- and 5-hr integration blocks with 3.5 GHz bandwidth (to account for RFI excision) centered at 6.0 GHz are 2.1 μJy and 1.4 μJy, respectively, and reach absolute flux calibration accuracy of ~5%.

To account for phase errors that can systematically reduce flux densities, the National Radio Astronomy Observatory (NRAO) previously recommended phase calibration cycle times of ~25 minutes for observations at 4–8 GHz in C configuration. We adhered to these guidelines for our observations. For GJ 564 BC, we alternated between a nearby phase calibrator and the target with integration times of 2 and 23.75 minutes, respectively, for a total cycle time of 25.75 minutes. For 2MASS J21402931+1625183, these integration times were 2 and 20.6 minutes, for a total cycle time of 22.6 minutes. For LP 415-20, the integration times were 2 and 23.5 minutes, for a total cycle time of 25.5 minutes. However, we note that NRAO recently updated their recommendations to cycle times of 10 minutes[1]. Consequently, our measured flux densities may suffer from some flux loss and the rms noise in the images may increase due to phase errors.

We self calibrate the target field for 2MASS J21402931+1625183 using a bright ~31.3 mJy object located at 21h40m35.12s +16d28'17''.87 and improve our

[1] https://science.nrao.edu/facilities/vla/docs/manuals/obsguide/calibration
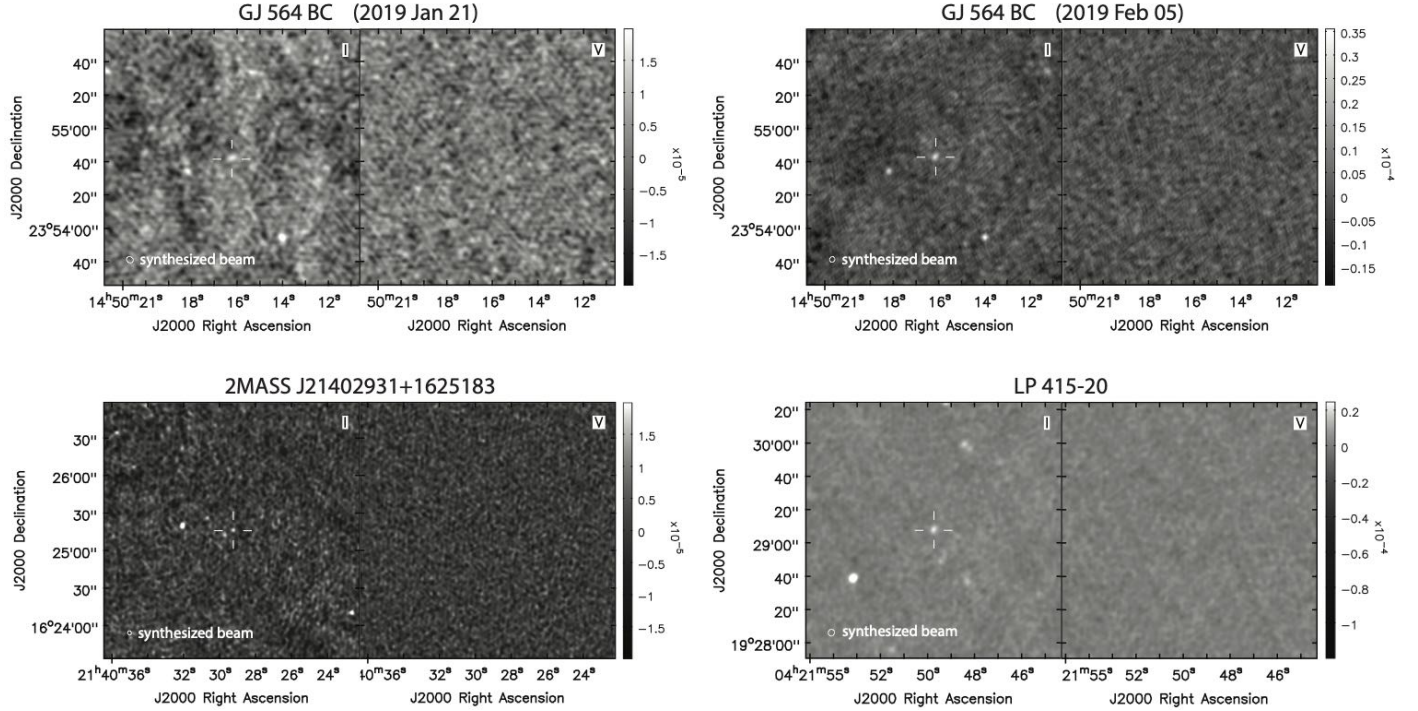
Figure 1. 4–8 GHz Stokes I and V images averaged over the full observing block for each target. Cross hairs indicate detected flux at the expected locations of our targets. No Stokes V emission was detected from our targets.

image rms noise by a factor of 12, from 43.4 μJy to 3.6 μJy.

We did not observe polarization calibrators, but the absence of polarization calibration is not a limiting factor for our analysis. Polarization leakage at typical levels of 2–3% result in spurious Stokes V (circularly polarized) flux densities of $\sim$1.2 μJy for our brightest source, which is less than the noise floor.

We initially processed each measurement set with the VLA CASA 5.6.2 Calibration Pipeline, after which we flagged all remaining radio frequency interference (RFI) and checked all calibrations. As a rule, all data between 4.0–4.4 GHz was discarded due to extremely bright and persistent RFI. We obtained absolute flux by bootstrapping flux densities with the observed flux calibrators.

2.3. Results: Imaging

We produced Stokes I and Stokes V (total and circularly polarized intensities, respectively) images for the entire observing block of each object with the CASA `tclean` routine. For GJ 564 BC and LP 415-20, we model the frequency dependence of sources with three terms to account for curvature in the spectrum. We also use natural weighting for best point-source sensitivity, multi-scale cleaning with a bias of 0.5 to more heavily weight point sources, and set the cell size to $0\rlap{.}''3 \times 0\rlap{.}''3$. For 2MASS J21402931+1625183, dynamic range limits

its imaging. To suppress sidelobes from bright sources in the field of view, we use Briggs weighting and set `robust = 0.5`. Bright sources outside of the primary beam cause image artifacts due to non-coplanar baselines. We mitigate these artifacts with w-projection and reduce some computational overhead by slightly increasing the cell size to $0\rlap{.}''4 \times 0\rlap{.}''4$. Finally, we model the frequency dependence of sources with four terms to account for artifacts that cannot be satisfactorily modeled with three terms.

We searched for a point source at the proper motion-corrected coordinates of each target by eye and detect radio emission from all three of our targets, including for both epochs of GJ 564 BC.

For each object, we fit the flux density of the source using two methods. Prior to flux fitting, we added phase delays to our visibility data to transform the phase center of our data to the measured locations of our targets using the CASA task `fixvis`. After cleaning the target field, we subtracted models for all sources except for the target using the CASA task `uvsub`. Then, we fit the calibrated visibilities with a point source model using the CASA task `uvmodelfit`. We also fit an elliptical Gaussian point source to the cleaned image of each object using the CASA task `imfit`. Table 2 gives measured flux densities and percent circular polarizations for detected objects and 3σ upper limits on the flux densities for undetected

Table 3. Flux density measurements

Object	Stokes I Peak F_ν uvmodelfit (μJy)	Peak F_ν imfit (μJy)	Integrated F_ν imfit (μJy)	$[L_\nu]^a$ (erg s^{-1} Hz^{-1})	Stokes V F_ν (μJy)	$[L_\nu]$ (erg s^{-1} Hz^{-1})	% Circ. Poln.^{a}	Notes
GJ 564 BC	22.7±2.7	19.4±4.5	21.6±8.7	12.9	<12.0	<12.7	$\leq 58.8^{+24.0}_{-19.6}$	Epoch: 2019 Jan 21
	31.3±2.2	30.1±3.7	38.7±7.6	13.1	<9.3	<12.6	$\leq 30.4^{+12.7}_{-9.8}$	Epoch: 2019 Feb 05
J2140+1625	15.6±1.7	20.1±3.3	16.0±5.0	13.4	<9.0	<13.4	$\leq 43.6^{+20.8}_{-13.8}$	
LP 415-20	24.1±1.4	22.9±2.5	24.9±4.6	13.6	<6.5	<13.1	$\leq 28.0^{+11.2}_{-9.1}$	

NOTE—We measured Stokes I flux densities in two ways: (1) fitting the cleaned image with the CASA task `imfit` and (2) fitting the uv visibilities with the task `uvmodelfit` after subtracting other sources in the primary beam. `imfit` returns both peak flux density and integrated flux density. For point sources, the peak flux density should be consistent with the integrated flux density. `uvmodelfit` returns formal errors that are underestimated by at least a factor $\sqrt{\chi^2_R}$, which we have corrected for in the reported errors. No Stokes V sources were detected, so we report the $3\sigma_{\rm rms}$ upper limit.

^{a} Calculated using the peak F_ν fitted with `imfit`. Uncertainties are less than the reported precision.

objects. Figure 1 shows Stokes I and V images for all targets.

2.4. *Results: Timeseries*

We also generated timeseries for each object's right- and left-circularly polarized (rr- and ll-correlations) emission. To do this, we time-averaged and frequency-averaged the phase-centered data into 10s, 30s, and 60s time resolutions each for 4–8 GHz, 4–6 GHz, and 6–8 GHz sub-bands using the averaging functions available with CASA's plotting tool `plotms`, and we exported the averaged timeseries of the real component of the phase-centered visibilities.

We then searched these timeseries for candidates of highly circularly polarized pulses indicative of auroral emission using the following revision of the procedure described in Kao et al. (2018):

1. Calculate a timeseries t_q for slowly varying quiescent emission by smoothing the raw timeseries with a Gaussian kernel that has a width of 10% of the total time on-source.

2. Construct a timeseries t_p for pulse-searching by smoothing the raw timeseries with a Gaussian kernel that has a width of 1% of the total time on-source. This mitigates anomalous noise spikes, which are much narrower than observed radio aurorae pulses that have durations at least as long as several minutes (e.g. Berger et al. 2001; Burgasser & Putman 2005; Hallinan et al. 2007, 2008; Berger 2006; Berger et al. 2009; Route & Wolszczan 2012, 2016b; Williams et al. 2015a; Gizis et al. 2016; Kao et al. 2016, 2018; Zhang et al. 2020).

3. Subtract t_q from t_s to obtain a residual timeseries t_r without the quiescent component.

4. Identify peaks with at least $2\sigma_{\rm rms}$, where $\sigma_{\rm rms}$ is the root mean square of t_r. This lower significance accounts for the possibility that t_r may have pulses that could elevate $\sigma_{\rm rms}$ and prevent the identification of weaker pulses. Thus, we remove the strongest peaks in the first iteration of this procedure and then repeat it with an updated $\sigma_{\rm rms}$ that excludes any initially identified peaks.

5. Calculate the full-width half-maximum (FWHM) of identified peaks.

6. Remove the full width of each identified peak from t_r, where we define the full width of each peak as three times the FWHM. This gives the updated residual timeseries $t_{r,u}$.

7. Repeat steps 4–6, using $t_{r,u}$ for calculating $\sigma_{\rm rms}$ and t_r for peak-searching. For this iteration, we also require a peak significance threshold of $3\sigma_{\rm rms}$. Returned peaks are candidate pulses. Note that by using t_r for the peak search, this procedure does not inherit identified peaks using the lower significance from the first iteration. Instead, all candidate pulses identified by the full procedure must meet a $3\sigma_{\rm rms}$ significance.

We emphasize that the sole function of the procedure outlined above is to aid in identifying candidate pulses in a repeatable manner. Final confirmation of identified candidate pulses relies on human judgement. Figure 2 shows the 4–8 GHz timeseries for each object.

We detect one candidate pulse from GJ 564 BC during its first epoch. Comparing the 4–6 GHz and 6–8 GHz timeseries shows that the pulse appears only in the lower subband (Figure 3). To confirm this pulse, we image over the time interval of its FWHM at 4–6 GHz and measure
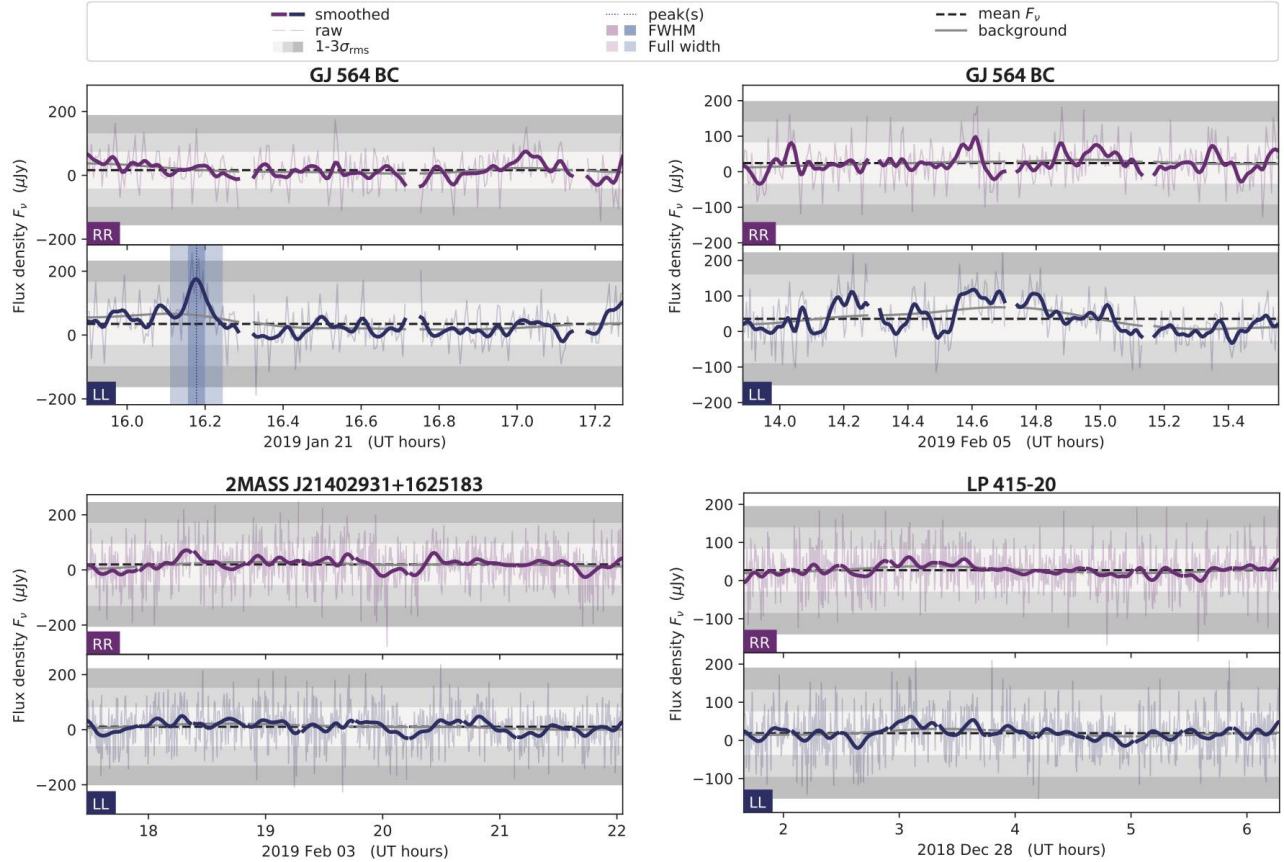
Figure 2. 4–8 GHz right- and left-circularly polarized (RR and LL, respectively) timeseries for detected objects with 10s averaging. Gaps in timeseries correspond to phase calibration scans and rms values shown correspond to the rms of the raw time-averaged data. A left circularly polarized candidate pulse was detected in the 2019 Jan 21 epoch for GJ 564 BC, and shaded regions around that pulse show the calculated FWHM and full width regions.

its Stokes I (95 ± 27 μJy) and Stokes V (125 ± 24 μJy) flux densities. While Stokes V flux densities cannot physically exceed Stokes I flux densities, the measured Stokes I and V flux densities are consistent within $3\sigma_{rms}$ and correspond to a lower bound percent circular polarization of $\geq38\%$ with 99.7% confidence. For comparison, imaging outside of the full width of the identified pulse using the full bandwidth yields a Stokes I quiescent emission flux density of 19.2 ± 4.9 μJy, and no Stokes V source is detected to a $3\sigma_{rms}$ significance of ≤15.0 μJy.

However, the target is difficult to distinguish from noise peaks in the image (Figure 4), so we bootstrap the significance of the measured Stokes I and Stokes V flux densities by fitting a point source in 10,000 randomly drawn fitting regions of size 50×50 pixels. We find that the Stokes I flux density has a significance of 98.5% and the Stokes V flux density has a significance of 99.9%. We therefore classify this candidate pulse as only a tentative detection. Similarly, the Stokes I flux density of the quiescent emission is also tentative, corresponding to a 99.8% significance.

We did not identify any candidate pulses from 2MASS J21402931+1625183 and LP 415-20 despite covering their likely full rotation periods. However, we note that our chosen time-averaging is only sensitive to pulses that are at least as bright as a peak flux of $\sim$100–200 μJy, or $\sim$5–10$\times$ brighter than their measured quiescent emission. Fainter pulses may exist to which our observations are not sensitive.

3. THE QUIESCENT RADIO OCCURRENCE RATE OF SINGLE OBJECTS VS. BINARIES

3.1. *Data*

To compare the radio occurrence rates of binary systems to single objects, we use the compilations of single objects in Kao & Shkolnik (submitted). This set includes 82 ultracool M dwarfs, 74 L dwarfs, and 23 T/Y dwarfs. We also compile all available measurements of *detected* quiescent radio emission from binary ultracool dwarfs in Table 4. We use the datasets containing all measurements of detected quiescent radio emission for single objects and binaries to define the luminosity priors

Table 4. Specific luminosities for detected quiescent radio emission in binary ultracool dwarf systems

Object Name	Other Name	SpT	π (mas)	d (pc)	ref	F_ν (μJy)	$\log_{10}(L_\nu)$	ref
GJ 564 BC	HD 130948B	L4+L4	54.9068±0.0684	18.2127±0.0227	30	19.4±4.5	12.9	1
						30.1±3.7	13.1	1
2MASS J21402931+1625183		M8+L0.5	30.1972±0.434	33.1157±0.4759	30	20.1±3.3	13.4	1
2MASS J00043484-4044058	GJ 1001 B	L5+L5	82.0946±0.3768	12.1811±0.0559	30	100.0±8.3	13.2	20
2MASS J00275592+2219328	LP349-25	M7+M8	69.2±0.9	14.5±0.2	13	262±40	13.8	23
						320±21	13.9	23
						338±54	13.9	23
						365±16	14.0	24
						383±27	14.0	23
2MASS J04234858-0414035	SDSS J042348.57-041403.5	L6.5+T2	67.8584±1.5052	14.7366±0.3269	30	15.4±1.2	12.6	19
						26.7±3.1	12.8	18
2MASS J12560183-1257276a	VHS J125601.92-125723.9a	M7.5+M7.5	78.8±6.4	12.7±1.0	15	60±3	13.1	16
2MASS J13153094-2649513AB		L3.5+T7	53.8729±1.1265	18.5622±0.3881	30	370±50	14.2	9
2MASS J13142039+1320011	NLTT 33370	M7.0+M7.0	57.975±0.045	17.2488±0.0134	12	1099±18	14.6	21
						1032±16	14.6	21
WISE J072003.20-084651.2AB		M9+T5	142±38	7±2	26	15±3	11.9	10

NOTE—This table does not include the M7+M7 binary 2MASS J09522188-1924319 due to possibility that the radio emission detected from this object may be flaring rather than quiescent emission. (McLean et al. 2012) detected 233 ± 15 muJy emission from this object, which corresponds to $[L_\nu] = 14.4$. However, they reported that followup observations at 4.96 and 8.46 GHz after the initial detection did not yield a detection to a limit of 69 μJy, or a factor of 2.4 below the original detection. They concluded that the initial detection was likely a flare or that 2MASS J09522188-1924319 exhibits long-term variability. We also exclude LP 415-20 because of compelling evidence that the primary component of this system may in fact be unresolved ultracool dwarf binaries (Dupuy & Liu 2017).

[a] Uncertainties are less than the reported precision and do not affect the presented analysis.

[b] McLean et al. (2012), Forbrich et al. (2016), and Williams et al. (2015a) also observe 2MASS J13142039+1320011 at radio frequencies but do not separately report quiescent emission.

References— (1) This paper ; (2) Berger et al. (2001) ; (3) Berger (2002) ; (4) Berger et al. (2005) ; (5) Berger (2006) ; (6) Berger et al. (2008b) ; (7) Berger et al. (2008a) ; (8) Berger et al. (2009) ; (9) Burgasser et al. (2013a) ; (10) Burgasser et al. (2015a) ; (11) Burgasser & Putman (2005) ; (12) Dupuy et al. (2016) ; (13) Dupuy & Liu (2017) ; (14) Faherty et al. (2012) ; (15) Gauza et al. (2015) ; (16) Guirado et al. (2018) ; (17) Hallinan et al. (2006) ; (18) Kao et al. (2016) ; (19) Kao et al. (2018) ; (20) Lynch et al. (2016) ; (21) McLean et al. (2011) ; (22) Osten et al. (2006) ; (23) Osten et al. (2009) ; (24) Phan-Bao et al. (2007) ; (25) Richey-Yowell et al. (accepted) ; (26) Scholz (2014) ; (27) Schmidt et al. (2010) ; (28) Williams et al. (2013) ; (29) Williams & Berger (2015) ; (30) Gaia Collaboration (2018)

Table 5. Radio Observations of Multi-object Ultracool Dwarf Systems from the Literature

Object Name	SpT	π (mas)	d (pc)	F_ν [b] (μJy)	ref	Note
2MASS J00244419-2708242	M6+M8.5+M9	132.3 ± 11.4	7.6 ± 0.7	<111.0	41 37 57 44	c
2MASS J00275592+2219328	M7+M8	69.2 ± 0.9	14.5 ± 0.2	323 ± 14	24 24 24 47	d
2MASS J04291842-3123568	M7.5+L1	59.3757 ± 0.2018	16.8 ± 0.06	<48	53 54 28 6	
2MASS J09522188-1924319	M7	34.5193 ± 0.1511	29.0 ± 0.13	233 ± 15	45 50 28 47	e
2MASS J11214924-1313084	M8.5+L7.5	69.4903 ± 0.176	14.4 ± 0.04	<102	3 24 28 47	
2MASS J12073346-3932539	M8+L5	19.1 ± 0.4	52.4 ± 1.1	<29	31 7 23 49	
2MASS J12560183-1257276 Aab	M7.5+M7.5	78.8 ± 6.4	12.7 ± 1.0	60 ± 3	29 29 29 33	f
2MASS J17072343-0558249	M9+L3	$\cdots$	7.0 ± 1.0	<48	51 46 26 6	
2MASS J22000201-3038327	M8+L0	41 ± 4	24.4 ± 2.4	<78	26 12 42 47	
2MASS J22062280-2047058	M8.0+M8.5	35.8 ± 1	27.9 ± 0.8	<84	20 24 24 47	
GJ 569 Bab	M8.5+M9	93.814 ± 0.724	10.7 ± 0.1	<30	38 24 28 6	g
WISE J072003.20-084651.2	M9+T5	147.1 $^{+1.1}_{-1.2}$	6.8 $^{+0.05}_{-0.06}$	15 ± 3	18 25 25 19	
2MASS J00043484-4044058	L5+L5	82.0946 ± 0.3768	12.2 ± 0.1	100 ± 8.3	51 32 28 44	h
2MASS J02052940-1159296	L5+L8+T0	50.6 ± 1.5	19.8 ± 0.6	<30	10 10 27 6	
2MASS J03105986+1648155	L9+L9	36.9 ± 3.4	27.1 ± 2.5	<10.8	35 56 55 52	
2MASS J04234858-0414035	L6.5+T2	67.8584 ± 1.5052	14.7 ± 0.3	54.1 ± 2.2	23 24 28 34	
2MASS J07003664+3157266	L3+L6.5	88.279 ± 0.3479	11.33 ± 0.04	<42	23 24 28 1	
2MASS J07464256+2000321 A	L0	80.9 ± 0.8	12.4 ± 0.1	71 ± 12	9 24 24 58	
2MASS J07464256+2000321 B	L1.5	80.9 ± 0.8	12.4 ± 0.1	128 ± 14	9 24 24 58	
2MASS J10491891-5319100	L7.5+T0.5	496 ± 37	2.0 ± 0.2	<15	17 40 43 48	
2MASS J12281523-1547342	L5.5+L5.5	48 ± 1.7	20.8 ± 0.7	<87	23 21 24 5	i
2MASS J13054019-2541059	L2+L3.5	53.8492 ± 0.7107	18.6 ± 0.2	<27.6	36 24 28 39	
2MASS J13153094-2649513	L3.5+T7	53.8729 ± 1.1265	18.6 ± 0.4	370 ± 50	14 15 28 16	
2MASS J14413716-0945590	L1+L1	31.6439 ± 1.0131	31.6 ± 1.0	<84	51 8 28 47	
2MASS J17114573+2232044	L5.0+T5.5	33.11 ± 4.81	30.2 ± 4.4	<11.4	13 4 27 52	
2MASS J17281150+3948593	L5+L6.5	36.4 ± 0.6	27.5 ± 0.5	<54	30 24 24 6	
2MASS J22521073-1730134	L4.5+T3.5	59.1461 ± 0.8244	16.9 ± 0.2	<30	23 24 28 6	
2MASS J15344984-2952274	T4.5+T5	63 ± 1.1	15.9 ± 0.3	<63	23 24 24 6	
2MASS J22041052-5646577 A	T1+T6	275.79 ± 0.69	3.63 ± 0.01	<79.2	11 22 43 2	j
2MASS J22041052-5646577 B	T1+T6	275.79 ± 0.69	3.63 ± 0.01	<79.2	11 22 43 2	

NOTE— Distances calculated from parallaxes are provided for the reader's convenience but are truncated to three significant figures in the interest of space. We report upper limits or flux densities as presented in the radio observation references and define detected = 1 if $F_\nu \geq 4.0$ to remain consistent with our occurrence rate calculation. Reference order: SpT, d, F_ν.

[c] We do not include 2MASS J00244419-2708242 in the binary calculation because the ATCA 6A configuration cannot resolve this triple system.

[d] McLean et al. (2012) list 2MASS J00275592+2219328 as LP 349-25 B, but the primary and secondary components of this binary are unresolved by the VLA. Thus, we list this observation for both components.

[e] Reid et al. (2002) report that 2MASS J09522188-1924319 is an unresolved double-lined spectroscopic binary, but Guenther & Wuchterl (2003) observed only a single line. We exclude this system due to the possibility that its detected radio emission may be flaring rather than quiescent emission (McLean et al. 2012).

[f] The discovery that the primary in the 2MASS J12560183-1257276 AB system is actually an equal-mass binary (Stone et al. 2016) suggests that this system may be as far as 17.1 ± 2.5 pc rather than the 12.7 ± 1.0 pc reported by Gauza et al. (2015). The wide $\geq 102 \pm 9$ AU separation between the primary and secondary components (Gauza et al. 2015) is easily resolved in all observations and precludes magnetic interactions between components, so we include 2MASS J12560183-1257276 Aab in the binary sample.

[g] GJ 569 Bab is a companion to an M3 primary that is separated by ∼53 AU. This corresponds to ∼5″(Forrest et al. 1988) and is resolved by the VLA. The wide separation precludes magnetic interactions between components, so we include GJ 569 Bab in the binary sample.

[h] 2MASS J00043484-4044058 (GJ 1001) is a triple system, in which the M4 primary is separated by ∼180 pc from the L5+L5 binary secondary (Golimowski et al. 2004). The observation reported here is for the binary component of the triple. This distance is easily resolved, so we include this observation in the binary sample. Golimowski et al. (2004) do not give error estimates for their measured angular separation.

[i] Dupuy & Liu (2017) note that the orbit fit for 2MASS J12281523-1547342 is of questionable quality.

[j] 2MASS J22041052-5646577 is also known as ϵ Ind Bab.

References— (1) Antonova et al. (2013) ; (2) Audard et al. (2005) ; (3) Bardalez Gagliuffi et al. (2014) ; (4) Bardalez Gagliuffi et al. (2015) ; (5) Berger (2002) ; (6) Berger (2006) ; (7) Blunt et al. (2017) ; (8) Bouy et al. (2003) ; (9) Bouy et al. (2004) ; (10) Bouy et al. (2005) ; (11) Burgasser et al. (2005) ; (12) Burgasser & McElwain (2006) ; (13) Burgasser et al. (2010) ; (14) Burgasser et al. (2011b) ; (15) Burgasser et al. (2011a) ; (16) Burgasser et al. (2013a) ; (17) Burgasser et al. (2013b) ; (18) Burgasser et al. (2015b) ; (19) Burgasser et al. (2015a) ; (20) Deshpande et al. (2012) ; (21) Dieterich et al. (2014) ; (22) Dieterich et al. (2018) ; (23) Dupuy & Liu (2012) ; (24) Dupuy & Liu (2017) ; (25) Dupuy et al. (2019) ; (26) Faherty et al. (2009) ; (27) Faherty et al. (2012) ; (28) Gaia Collaboration (2018) ; (29) Gauza et al. (2015) ; (30) Gelino et al. (2014) ; (31) Gizis (2002) ; (32) Golimowski et al. (2004) ; (33) Guirado et al. (2018) ; (34) Kao et al. (2016) ; (35) Kirkpatrick et al. (2000) ; (36) Koen (2013) ; (37) Köhler et al. (2012) ; (38) Konopacky et al. (2010) ; (39) Krishnamurthi et al. (1999) ; (40) Lazorenko & Sahlmann (2018) ; (41) Leinert et al. (2000) ; (42) Liu et al. (2016) ; (43) Luhman (2013) ; (44) Lynch et al. (2016) ; (45) McCaughrean et al. (2002) ; (46) McElwain & Burgasser (2006) ; (47) McLean et al. (2012) ; (48) Osten et al. (2015) ; (49) Osten & Jayawardhana (2006) ; (50) Reid et al. (2002) ; (51) Reid et al. (2008) ; (52) Richey-Yowell et al. (accepted) ; (53) Schmidt et al. (2007) ; (54) Siegler et al. (2005) ; (55) Smart et al. (2013) ; (56) Stumpf et al. (2010) ; (57) Weinberger et al. (2016) ; (58) Zhang et al. (2020)
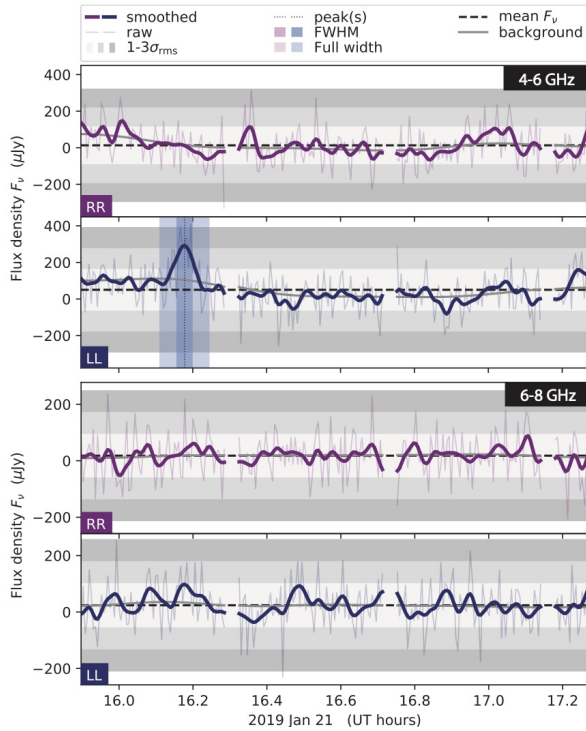
Figure 3. 4–6 GHz and 6–8 GHz right- and left-circularly polarized (RR and LL, respectively) timeseries for GJ 564 BC. Shaded regions around that pulse show the calculated FWHM and full width regions. The candidate pulse appears to drop out at 6–8 GHz.

that we assume for our occurrence rate calculations in §3.4.2.

Finally, we performed a literature search to compile a list of all radio observations, *including non-detections*, of ultracool dwarf binaries with individual components that have spectral type ≥M7. Some objects have been observed multiple times, so we follow the data inclusion policy described in Kao & Shkolnik (submitted) to produce a data set that represents observations that are independent from each other. In this data set, each object is represented only once. For each non-detected object, we select its most sensitive observation. For each detected object, we select the detection with the lowest rms noise. Furthermore, the flux densities that we list correspond to quiescent emission and exclude contributions from identified flares. This latter dataset serves as the input dataset for our occurrence rate calculations in §3.5.

Our binary sample contains 28 systems, summarized in Table 5. For binaries with reported radio emission for separate components, we choose the higher rms value to be conservative and designate the binary as detected if at least one component was detected. We include only binary systems for which both components are ultracool dwarfs and exclude triples except for hierarchical systems in which observations resolve the binary. For the triple
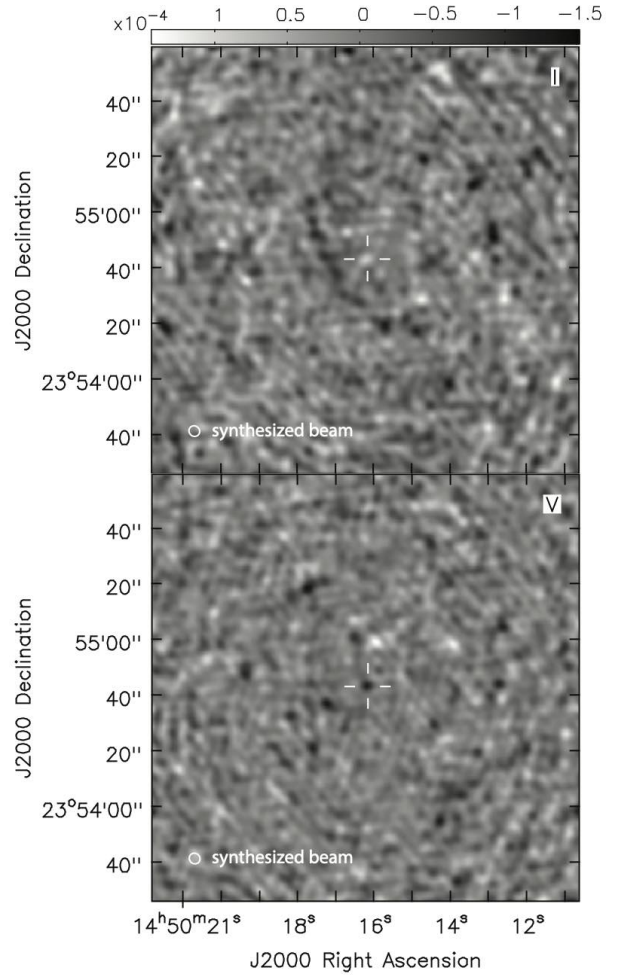
Figure 4. Image of GJ 564 BC over the FWHM of its identified candidate pulse. The target is visually indistinguishable from noise peaks in Stokes I and marginally distinguishable in Stokes V. Bootstrapping yields a significance of 98.5% for the Stokes I flux density and 99.9% for the Stokes V flux density. We classify this pulse as tentative rather than confirmed.

system 2MASS J12560183-1257276, we include the primary component, an M7.5+M7.5 close-in binary system (Stone et al. 2016). We exclude the L7.0 secondary component due to its wide ≥ 102 ± 9 AU separation (Gauza et al. 2015), which is more than ∼30 times the separation between the Sun and Jupiter and is easily resolved in all observations. Given its large separation, we include it in the single-object sample instead. Similarly, we include the binary system 2MASS J00043484-4044058 BC (GJ 1001 BC) and ε Ind Bab. These systems are part of widely-separated triple systems in which the primary components are separated from the secondary binary systems by ∼180 AU (18″, Golimowski et al. 2004) and ∼1459 AU (402″, Scholz et al. 2003). Finally, we also include GJ 564 BC. Although it resides in a triple system, the primary component is a solar analog at a distance

of ∼47 AU (Potter et al. 2002; Dupuy et al. 2009). This separation is not resolvable by the VLA for our observations, but solar radio emission from 4–8 GHz during solar maximum at this object's distance is not detectable by the VLA (Villadsen et al. 2014). Since the primary components of these systems are not ultracool dwarfs and are M4, K5V, and G2V stars, respectively, we do not include the primaries in the single sample.

We exclude from our sample LP 415-20 because of compelling evidence that the primary component of this system may in fact be unresolved ultracool dwarf binaries (Dupuy & Liu 2017). The primary is not resolvable from its secondary. We additionally exclude GJ 569 Bab, which is in a triple and separated from its M3 primary by ∼50 AU (5″, Forrest et al. 1988). Although Berger (2006) do not report the observation date, VLA configuration, or observing frequency for this target, we surmise from an archive search that this target was observed during VLA B configuration at C band (Project Code AB1179, PI Bower). The separation between GJ 569 Bab and its primary is resolvable by the VLA for this observation. However, the stellar wind properties of M dwarfs are not well known, so we cannot be confident that GJ 569 Bab remains largely uninfluenced by its primary star at this separation. Finally, we exclude the M7+M7 binary 2MASS J09522188-1924319 due to the possibility that the radio emission detected from this object may be flaring rather than quiescent emission. McLean et al. (2012) detected 233 ± 15 μJy emission from this object, which corresponds to $[L_\nu] = 14.4$. However, they reported that followup observations at 4.96 and 8.46 GHz after the initial detection did not yield a detection to a limit of 69 μJy, or a factor of 2.4 below the original detection. They concluded that the initial detection was likely a flare or that 2MASS J09522188-1924319 exhibits long-term variability.

3.2. Adapting the Kao & Shkolnik (submitted) occurrence rate framework to binary systems

Does binarity affect the magnetic activity of ultracool dwarfs? To answer this question, we compare the quiescent radio occurrence rates for ultracool dwarfs in single-object versus binary systems by adapting the occurrence rate framework developed by Kao & Shkolnik (submitted).

This occurrence rate framework for single objects considers the probability θ_{single} that an object is emitting between an assumed luminosity range $L_\nu \in [L_{\min}, L_{\max}]$ for a dataset D consisting of individual observations where the ith observation $D_i = \{\mathrm{detect}_i, \sigma_{\mathrm{rms}_i}, d_i, \sigma_{d_i}, L_{\nu,i}\}$. They treat each observation property as a random variable, where $\mathrm{detect}_i \in \{0 \text{ if undetected}, 1 \text{ if detected}\}$, σ_{rms_i} is the reported rms noise for each object, d_i is the distance to each object, σ_{d_i} is the error for the measured d_i, and $L_{\nu,i}$ is the assumed specific luminosity for quiescent radio emission. They show that for single-object systems, the probability $\mathbb{P}(D \mid \theta_{\mathrm{single}})$ of observing a dataset given a fixed occurrence rate $\theta_{\mathrm{single}} = \Theta$ depends on the probability of drawing the particular observational and object properties captured in D:

$$\mathbb{P}(D \mid \theta_{\mathrm{single}} = \Theta) = \prod_{i=1}^{N} \mathbb{P}(\sigma_{\mathrm{rms}_i}) \, \mathbb{P}(\sigma_{d_i}) \, \mathbb{P}(d_i) \times \begin{cases} \Theta \, \mathbb{P}(L_{\nu,i} \geq L_{\mathrm{thr,i}} \mid \sigma_{\mathrm{rms}_i}, \sigma_{d_i}, d_i, e = 1) & , \; \mathrm{detect}_i = 1 \\ 1 - \Theta \, \mathbb{P}(L_{\nu,i} \geq L_{\mathrm{thr,i}} \mid \sigma_{\mathrm{rms}_i}, \sigma_{d_i}, d_i, e = 1) & , \; \mathrm{detect}_i = 0 \end{cases} \quad (1)$$

where $\mathbb{P}(L_{\nu,i} \geq L_{\mathrm{thr,i}} \mid \sigma_{\mathrm{rms}_i}, \sigma_{d_i}, d_i, e = 1)$ is the probability that the object has a detectable luminosity and $e \in \{0 = \text{not emitting}, 1 = \text{emitting}\}$ denotes whether or not an object is emitting within the luminosity range of interest. Note that here we use distance and parallax interchangeably, and Kao & Shkolnik (submitted) provide the algebra for using either. In the analysis that we present in §3.6, we use parallaxes when available and distance estimates otherwise.

Kao & Shkolnik (submitted) describe how to calculate $\mathbb{P}(\sigma_{\mathrm{rms}_i})$, $\mathbb{P}(\sigma_{d_i})$, and $\mathbb{P}(d_i)$. These remain the same for unresolved binary systems. They additionally describe how to calculate $\mathbb{P}(L_{\nu,i} \geq L_{\mathrm{thr,i}} \mid \sigma_{\mathrm{rms}_i}, \sigma_{d_i}, d_i, e = 1)$ for single objects. This quantity requires a luminosity distribution for emitting objects $\mathcal{P}(L_{\nu,\mathrm{single}} \mid e = 1)$ within the assumed luminosity range of interest $L_{\nu,\mathrm{single}} \in [L_{\nu,\min}, L_{\nu,\max}]$. The only change required for applications to unresolved binary systems is replacing $\mathcal{P}(L_{\nu,\mathrm{single}} \mid e = 1)$ with the luminosity distribution of unresolved binary systems given that the system is emitting, $\mathcal{P}(L_{\nu,\mathrm{binary}} \mid e = 1)$. For the remainder of this section, we address $\mathcal{P}(L_{\nu,\mathrm{binary}} \mid e = 1)$.

For single objects, $\mathcal{P}(L_{\nu,\mathrm{single}} \mid e = 1)$ does not depend on the occurrence rate. Furthermore, it does not require any assumptions about how probability mass is distributed for $L_{\nu,\mathrm{single}} \notin [L_{\nu,\min}, L_{\nu,\max}]$ outside of the luminosity range of interest.

However, for unresolved multi-object systems, we must consider the full luminosity distribution $\mathcal{P}(L_{\nu,\mathrm{single}})$ for single objects. The occurrence rate now refers to that of unresolved binary systems θ_{binary} rather than the individual components of binary systems. Consequently, the luminosity prior $\mathcal{P}(L_{\nu,\mathrm{binary}} \mid e = 1)$ must refer to that of unresolved

binary systems given that each system as a whole is emitting between the assumed luminosity range of interest. For comparisons to single-object systems, care must be taken to ensure an apples-to-apples comparison.

In particular, we must construct $\mathcal{P}(L_{\nu,\mathrm{binary}} \mid e = 1)$ within the context of the luminosity distribution for single objects $\mathcal{P}(L_{\nu,\mathrm{single}})$. This is because unresolved binaries emit when one or both of their components are emitting. Furthermore, they can satisfy the emission threshold even if both components are individually too faint to meet the emission threshold. We discuss this additional caveat in §3.3. Thus, we must account for all cases.

The luminosity for an unresolved binary is equal to the summed luminosities of the a and b components such that $L_{\nu,\mathrm{binary}} = L_{\nu,a} + L_{\nu,b}$. We assume that the luminosities for the individual components each follow the distribution $\mathcal{P}(L_{\nu,\mathrm{single}})$, which gives the convolution

$$\mathcal{P}(L_{\nu,\mathrm{binary}}) = \begin{cases} \mathcal{P}(L_{\nu,\mathrm{single}}) * \mathcal{P}(L_{\nu,\mathrm{single}}) & , \ 0 \leq L_{\nu,\mathrm{binary}} \leq 2L_{\nu,\mathrm{max}} \\ 0 & , \ \mathrm{otherwise} \quad . \end{cases} \tag{2}$$

Notice that this extends possible luminosities for $\mathcal{P}(L_{\nu,\mathrm{binary}})$ to higher luminosities. Accordingly, the binary luminosity range of interest for $e = 1$ becomes $L_{\nu,\mathrm{binary}} \in [L_{\nu,\mathrm{min}}, 2L_{\nu,\mathrm{max}}]$. Here, the probability mass for $\mathcal{P}(L_{\nu,\mathrm{single}})$ is distributed such that

$$\int_{L_{\mathrm{min}}}^{L_{\mathrm{max}}} \mathcal{P}(L_{\nu,\mathrm{single}}) = \theta_{\mathrm{single}} \tag{3}$$

and the remaining probability mass $1 - \theta_{\mathrm{single}}$ is distributed over $L_{\nu,\mathrm{single}} \notin [L_{\nu,\mathrm{min}}, L_{\nu,\mathrm{max}}]$.

When we consider the case that both components are emitting, the distribution of probability mass $1 - \theta_{\mathrm{single}}$ outside of $L_{\nu,\mathrm{single}} \notin [L_{\nu,\mathrm{min}}, L_{\nu,\mathrm{max}}]$ becomes relevant. For instance, an individual object that is emitting at $L_{\nu,\mathrm{single}} = 0.8L_{\mathrm{min}}$ is not considered "emitting" in the single-object framework. In contrast, if both components in a binary are emitting at that luminosity, the binary luminosity $L_{\nu,\mathrm{binary}} = 1.6L_{\mathrm{min}}$ is within the binary luminosity range of interest. In §3.4, we discuss our choice for distributing the non-emitting probability mass $1 - \theta_{\mathrm{single}}$.

We can now re-write Eq. 1 to:

$$\mathbb{P}(D \mid \theta_p = \Theta) = \prod_{i=1}^{N} \mathbb{P}(\sigma_{\mathrm{rms}_i}) \, \mathbb{P}(\sigma_{\mathrm{d}_i}) \, \mathbb{P}(d_i) \, \mathbb{P}(p) \times \begin{cases} \Theta \, \mathbb{P}(L_{\nu,i} \geq L_{\mathrm{thr,i}} \mid \theta_p = \Theta, p, \sigma_{\mathrm{rms}_i}, \sigma_{\mathrm{d}_i}, d_i, e = 1) & , \ \mathrm{detect}_i = 1 \\ 1 - \Theta \, \mathbb{P}(L_{\nu,i} \geq L_{\mathrm{thr,i}} \mid \theta_p = \Theta, p, \sigma_{\mathrm{rms}_i}, \sigma_{\mathrm{d}_i}, d_i, e = 1) & , \ \mathrm{detect}_i = 0 \end{cases} . \tag{4}$$

Here, we have also added the multiplicative term $\mathbb{P}(p)$, or the probability that an object is in a given population p, where $p \in [\mathrm{single}, \mathrm{binary}]$. This allows us to condition on the appropriate luminosity distribution for each population. Notice that the probability that an emitting object's radio luminosity is detectable now depends on the assumed binary radio occurrence rate, and by implication, the single-object radio occurrence rate.

3.3. *Constructing a predicted binary occurrence rate $\theta_{predict}$ from the single-object occurrence rate θ_{single}*

To compare single objects to binary systems, we must consider the appropriate change of variables from the single-object occurrence rate θ_{single} to a predicted binary occurrence rate $\theta_{\mathrm{predict}}$. We can then compare the binary occurrence rate θ_{binary} to $\theta_{\mathrm{predict}}$. In Eq. 4, θ_{binary} refers to the occurrence rate of binaries in which the sum of both components fall into the binary luminosity range of interest such that

$$\theta_{\mathrm{binary}} = \mathbb{P}((L_a + L_b \geq L_{\mathrm{min}}) \cap (L_a + L_b \leq L_{\mathrm{max}})) \quad . \tag{5}$$

By choosing an appropriate L_{max} such that the single-object luminosity prior takes the form

$$\mathcal{P}(L_{\nu,\mathrm{single}}) = \begin{cases} 0 & , \quad L_{\nu,\mathrm{single}} > L_{\nu,\mathrm{max}} \\ \theta_{\mathrm{single}} \, \mathcal{F}_1(L_{\nu,\mathrm{single}}) & , \quad L_{\nu,\mathrm{single}} \in [L_{\nu,\mathrm{min}}, L_{\nu,\mathrm{max}}] \\ (1 - \theta_{\mathrm{single}}) \, \mathcal{F}_2(L_{\nu,\mathrm{single}}) & , \quad L_{\nu,\mathrm{single}} < L_{\nu,\mathrm{min}} \quad , \end{cases} \tag{6}$$

where $\mathcal{F}_1(L_{\nu,\mathrm{single}})$ and $\mathcal{F}_2(L_{\nu,\mathrm{single}})$ are density functions that depend on $L_{\nu,\mathrm{single}}$, Eq. 5 simplifies to $\theta_{\mathrm{binary}} = \mathbb{P}(L_a + L_b \geq L_{\mathrm{min}})$. Note that

We use Eq. 5 to construct θ_{predict} by assuming that binarity does not affect the radio occurrence rate of individual components. We also assume that the luminosities of each binary's individual components are drawn from the single-object luminosity distribution $\mathcal{P}(L_{\nu,\text{single}})$. In §3.4, we examine this latter assumption. We can then account for all combinations of $L_a + L_b$ by invoking the law of total probability and integrating

$$\theta_{\text{predict}} = \int_0^{L_{\max}} \mathbb{P}(L_a + k \geq L_{\min})\mathcal{P}(L_b = k)\, dk \tag{7}$$

$$= \int_0^{L_{\max}} \mathbb{P}(L_a \geq L_{\min} - k)\mathcal{P}(L_b = k)\, dk \quad , \tag{8}$$

where $\mathcal{P}(L_b = k)$ is the probability density distribution that the b component has a luminosity equal to k. This distribution is our chosen single-object luminosity distribution, such that $\mathcal{P}(L_b = k) = \mathcal{P}(L_{\nu,\text{single}} = k)$, and it gives the relationship between θ_{single} and θ_{predict}. Eq. 8 simplifies to

$$\theta_{\text{binary}} = C(\theta_{\text{single}}) + 1 - (1 - \theta_{\text{single}})^2 \quad , \tag{9}$$

where $C(\theta_{\text{single}})$ is a correction factor. When the non-emitting probability mass is a delta function at zero, $C(\theta_{\text{single}}) = 0$ because the radio occurrence rate for binaries is one minus the probability that neither component is emitting. When the mass is not distributed as a delta function, $C(\theta_{\text{single}})$ is positive and accounts for the additional pairs of objects that may be too faint individually to fall above $L_{\nu,\text{single}} \geq L_{\min}$ but together are luminous enough to fall above $L_{\nu,\text{binary}} \geq L_{\min}$. From Eq. 9, we expect that unresolved binaries are more likely to emit radio emission than their single counterparts when all else is equal.
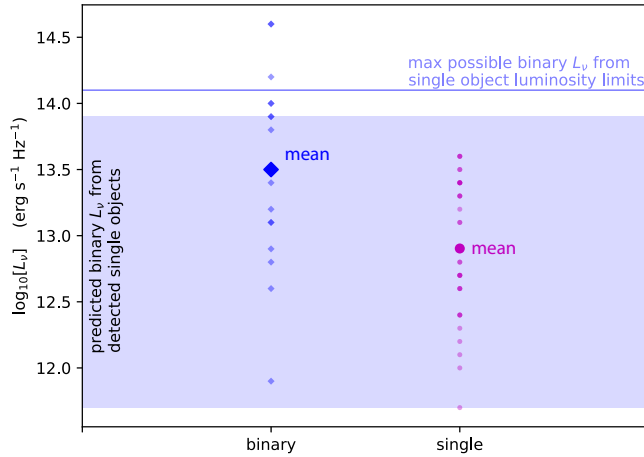
Figure 5. Radio luminosities of detected quiescent radio emission from ultracool dwarfs (translucent small markers) and mean values for binary versus single objects (solid big markers). Uncertainties are less than marker sizes. Shaded region corresponds to predicted binary luminosity ranges if individual binary components follow the same luminosity distribution as single objects. Line corresponds to the maximum possible binary luminosity limits of undetected single objects within 35 pc. Binary ultracool dwarfs are on average more radio luminous than single objects, and the brightest binaries may be overly luminous compared to predictions from single ultracool dwarfs.

3.4. Defining the luminosity distribution $\mathcal{P}(L_{\nu,single})$

3.4.1. Do individual binary components follow the same luminosity distribution as single objects?

As described in §3.2, self-consistent comparisons between single and binary systems require a binary luminosity prior constructed from that of single objects. One consequence of our treatment is that we expect binary systems to be more luminous on average than single objects when all else is equal. Indeed, the data seem to support this assumption. Figure 5 shows that the mean quiescent radio luminosities of detected binaries are brighter than detected single objects.

Intriguingly, the brightest binary systems may exceed luminosities predicted from single objects. We expect that binary luminosities will not exceed two times the maximum luminosity of single objects (Eq. 2) if binarity does not affect the luminosities of individual binary components. In Figure 5, we show that the brightest detected single systems cannot account for the high luminosities of the brightest detected binaries. This figure accounts for an individual object's intrinsic variability by including measurements from repeated observations of detected objects.

Similarly, we show that the distribution of detected single-object luminosities cannot account for that of binaries. In Figure 6, we construct the empirical cumulative distribution functions (ECDF) and 95% confidence intervals for detected single objects and binaries using the Kaplan-Meier estimator. The Kaplan-Meier estimator is a non-parametric statistic that is used in survival analysis
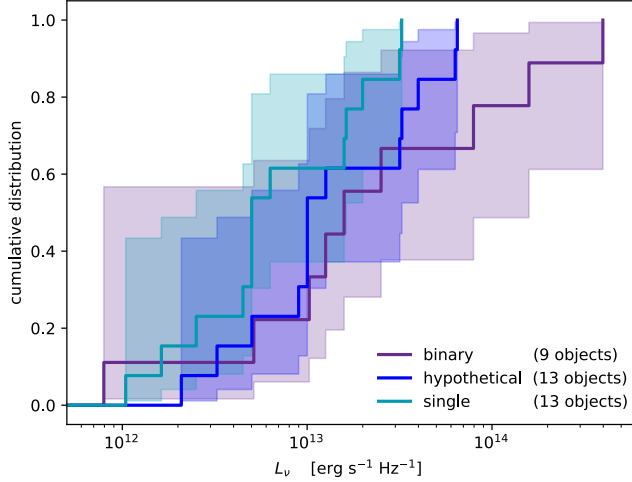
Figure 6. Empirical cumulative distribution function for detected single objects (teal), a hypothetical set of binaries that have $L_\nu = 2L_{\nu,\text{single}}$ (blue), and detected binary systems (purple). Shaded regions are 95% confidence intervals. For objects with more than one measurement, we use the median value. The 9 binary systems account for 16 total measurements. The 13 single objects account for 33 measurements.

Figure 7. Empirical cumulative distribution function for all observed single objects that meet the data inclusion criteria of Kao & Shkolnik (submitted) (teal), a hypothetical set of binaries that have $L_\nu = 2L_{\nu,\text{single}}$ (blue), and detected binary systems (purple) within 35 pc. Shaded regions are 95% confidence intervals. Detected objects with more than one measurements are represented with their median value. Distributions and confidence intervals are the mean distributions from 1000 trials in which we randomly draw single objects to match the spectral type distribution of the binary systems. The low luminosity end of the binary distribution is consistent with the single-object distribution, and the high luminosity end is consistent with the hypothetical distribution.

(Kaplan & Meier 1958; Lee & Wang 2003). For our case, it estimates the probability that an object in a given population is at most as bright as a given luminosity.

The set of all quiescent radio emission detections includes measured quiescent (non-flaring) radio luminosities for all observations of detected objects, including follow-up observations. This set includes 13 detected single objects that have a total of 33 measurements, as well as 9 binary systems that have 16 measurements between them. For objects with repeated observations, we use the median measured luminosity. We treat binaries as unresolved systems by combining the reported luminosities for 2MASS J07464256+2000321AB, for which resolved observations using the Very Long Baseline Array show both components are emitting (Zhang et al. 2020). An ECDF constructed from this dataset may be skewed from the true underlying luminosity distribution due to the small number of detected objects.

In Figure 6, we also construct an ECDF for hypothetical best-case unresolved binary systems that are twice as luminous as single objects by multiplying detected single-object luminosities and luminosity limits by a factor of two. For low luminosities, the actual binary distribution is consistent with the single-object and hypothetical distributions. However, we find that the brightest single systems cannot account for the high luminosities of the brightest binaries.

Finally, we construct an ECDF using the full set of compiled observations from the literature for objects that are within 35 pc, including non-detections. This

distance cutoff is consistent with all detected objects that we include in our samples, and it includes 151 and 25 single and binary systems, respectively, or 84% and 86% of observed systems.

The Kaplan-Meier estimator can account for upper limits by treating non-detections as left-censored data. However, the estimator makes the fundamental assumption that all objects in the given data set are emitting radio emission, even if it is not detectable. This assumption may not be true, since some undetected objects may not be emitting at all.

For the left-censored ECDF, each object is represented only once, and included upper limits correspond to the most sensitive observation that is available in the literature for that object. We use the median luminosity for objects with detected objects.

By using the full set of available data, we can control for spectral type effects. To do this, we randomly draw objects from the single-object sample to match the spectral type distribution of the individual components in the binary sample. We repeat this trial 1000 times and show the mean distribution and 95% confidence interval in Figure 7. We find that the low luminosity end of the binary distribution is consistent with the single-object
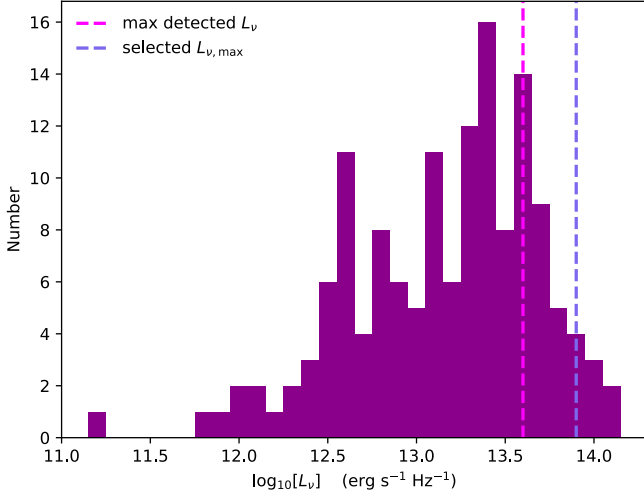
Figure 8. Histogram of 4σ luminosity limits for undetected single objects with 3σ distances within 35 pc. 85% of single-object observations had luminosity limits that would have been sufficient to detect the brightest quiescent radio emission observed in single objects.

distribution, and the high luminosity end is consistent with the hypothetical binary distribution.

This result depends in part on the distribution of upper limits. Figure 8 shows a histogram of 4σ sensitivity limits for all undetected single object systems with radio observations that have 3σ distances within 35 pc. $\sim$15–20% of objects may not be emitting above $10^{11.7}$ erg s^{-1} Hz^{-1} (Kao & Shkolnik submitted), so future observations at higher sensitivities may yield a significant number of upper limits at lower luminosities. In this case, we expect a significant portion of the probability mass in the ECDFs for the single and hypothetical populations to shift leftward to lower luminosities.

With the existing data available in the literature, we cannot conclusively determine if the binary population is overly luminous compared to predictions from their single counterparts. Thus, for our analysis, we default to Occam's razor and do not condition the underlying single-object luminosity distribution $\mathcal{P}(L_{\nu,\mathrm{single}})$ on binarity.

3.4.2. *Choosing a self-consistent luminosity distribution*

We focus on asking whether binaries have elevated radio occurrence rates relative to *analogous* single objects. To answer this question, we must use a luminosity distribution that is consistent for both the single and binary populations. Since detected binaries can be more luminous than predictions from detected single objects, we cannot adopt the same luminosity prior over the minimum and maximum observed single-object luminosities that Kao & Shkolnik (submitted) used. Instead, we must revise the luminosity range.

First, we choose $L_{\nu,\mathrm{max}}$ such that all empirical detections of single objects have $L_{\nu,\mathrm{single}} \leq L_{\nu,\mathrm{max}}$ and it reasonably accounts for detection limits. Twice the brightest reported quiescent radio luminosity for single objects corresponds to $[L_\nu] \sim 13.9$ erg s^{-1} Hz^{-1}, but the M7+M7 binary 2MASS J13142039+1320011 (also known as NLTT 33370 AB) has luminosities up to $[L_\nu] \sim 14.6$ erg s^{-1} Hz^{-1} (McLean et al. 2011). Surprisingly, resolved observations demonstrate that only one component of this system is emitting (Forbrich et al. 2016). This further underscores the possibility that individual components in binary systems may be overluminous compared to single-object systems. However, radio luminosities for this system can differ by greater than a factor of 2 (Williams et al. 2015a; Forbrich et al. 2016), and some portion of its radio emission has been attributed to gyrosynchrotron flares (Williams et al. 2015a).

Since the radio luminosity of 2MASS J13142039+1320011 may not trace solely quiescent radio emission, we turn to the next most luminous binary system, 2MASS J13153094-2649513AB. This L3.5+T7 binary has $[L_\nu] \sim 14.2$ erg s^{-1} Hz^{-1} (Burgasser et al. 2013a), which is still overly luminous compared to the brightest single objects.

Thus, for this calculation, we choose $[L_{\nu,\mathrm{max}}] = 13.9$ for single objects. This upper limit, revised from 13.6, is consistent with reported binary luminosities and it includes 97% of luminosity limits for single objects within 35 pc. Finally, it corresponds to twice the maximum quiescent radio luminosity of detected ultracool dwarfs, which is consistent with observed levels of variability in ultracool dwarf quiescent radio emission (Kao & Shkolnik submitted, and references therein). The one outlier is the L2.5 dwarf 2MASS J05233822-1403022, which Antonova et al. (2007) report can vary by a factor of $\sim$5 from $\leq$45 to 230$\pm$17 μJy with no evidence of short-duration flares during 2-hr observing blocks. Although the low circular polarization of this object rules out coherent aurorae, non-auroral flares at both radio and optical frequencies can persist for at least several hours (e.g. Villadsen & Hallinan 2019; Paudel et al. 2018b). This outlier object has been excluded from the single-object sample by Kao & Shkolnik (submitted) on the basis of the uncertain nature of its radio emission, similar to our reasoning for excluding the binary 2MASS J09522188-1924319.

Following Kao & Shkolnik (submitted), we assume two luminosity distributions for our calculations:

- **Uniform$_{e=1}$:** Emitting single objects have radio luminosities that are uniformly distributed between $L_{\nu,\mathrm{single}} \in [L_{\nu,\mathrm{min}} = 11.7, L_{\nu,\mathrm{max}} = 13.9]$. Here, $L_{\nu,\mathrm{min}}$ corresponds to the minimum detected radio luminosity for single ultracool dwarfs, and our
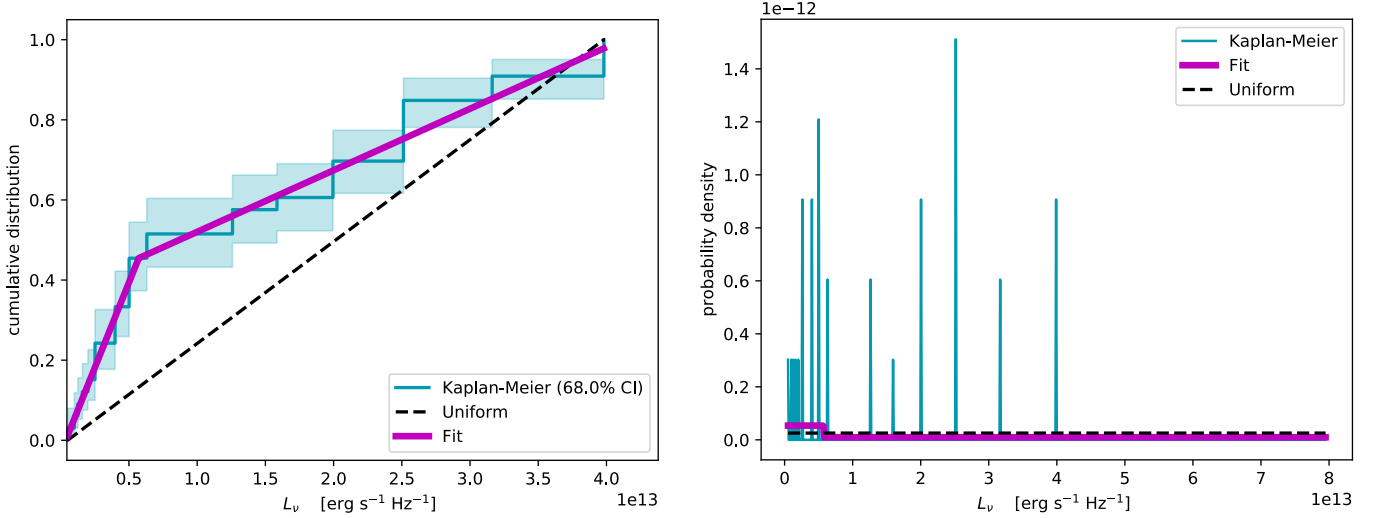
Figure 9. Left: The empirical cumulative distribution function for L_ν for all radio detections of single ultracool dwarfs, calculated using the Kaplan-Meier estimator (teal). Right: The probability density distribution calculated from the cumulative distribution function of single-objects, with the fitted piece-wise linear prior $\mathcal{P}(L_{\nu,\mathrm{single}} \mid e = 1)$ (magenta) and a uniform prior (black) extended to the full luminosity range that we choose and renormalized. We run calculations for both the distributions.

chosen $L_{\nu,\mathrm{max}}$ provides an upper bound for existing detection measurements. By including repeat observations of the same object, we can account for the intrinsic variability of individual objects. Calculations that use this luminosity distribution assume that our only prior knowledge about the luminosity distribution are the minimum and maximum values, as is the case with the existing limited data.

- **KM$_{e=1}$:** Alternatively, we can assume that emitting objects follow the same luminosity distribution of *all measured detections*. We construct this prior by fitting the Kaplan-Meier ECDF of emitting single objects with a piece-wise linear function (Figure 9) and differentiating the fitted function. This prior also accounts for intrinsic variability in individual objects, but it may be skewed from the true underlying luminosity distribution due to the non-uniformity of repeated observations and small sample size (33 measurements). The KM probability density distribution initially extends only to $[L_\nu] = 13.6$ erg s^{-1} Hz^{-1}, but it is characterized by two concatenated uniform distributions (Figure 9). Accordingly, we extend the luminosity distribution to our chosen maximum limit $[L_\nu] = 13.9$ erg s^{-1} Hz^{-1} and re-normalize.

Figure 9 shows our chosen luminosity priors for $\mathcal{P}(L_{\nu,\mathrm{single}} \mid e = 1)$. Using the same luminosity priors for both the single and binary populations controls for luminosity differences between single and binary popula-

tions and allows us to ask whether binaries have elevated occurrence rates relative to analogous single objects.

As discussed in §3.2, the probability mass outside of the luminosity prior for emitting single objects ($e = 1$) impacts the probability distribution for the binary luminosities. The single-object radio occurrence rate θ_{single} corresponds to the probability that an object is emitting within the assumed luminosity bounds $[L_{\nu,\mathrm{single}}] \in [11.7, 13.9]$ erg s^{-1} Hz^{-1}. Thus, we attribute θ_{single} of the probability mass for $\mathcal{P}(L_{\nu,\mathrm{single}})$ within these assumed bounds. Finally, we must decide how to distribute the rest of the probability mass $(1 - \theta_{\mathrm{single}})$ between $[L_{\nu,\mathrm{single}}] \in [0, 11.7)$ erg s^{-1} Hz^{-1}.

For this work, we examine the case where $(1 - \theta)$ of the mass is located at $L_{\nu,\mathrm{single}} = 0$. This simplest case equivalently assumes that single ultracool dwarfs only emit radio emission between $[L_{\nu,\mathrm{single}}] \in [11.7, 13.9]$ erg s^{-1} Hz^{-1}.

Our assumption is motivated by the fact that a number of factors can contribute to a lack of quiescent radio emission from a given ultracool dwarf. Such factors include but are not limited to the absence of a plasma source, magnetic fields that may not be sufficient in size or strength to confine the plasma, or the absence of a mechanism that can accelerate magnetospheric plasma to the mildly relativistic energies required for gyrosynchrotron emission. Indeed, planets demonstrate that not all objects meet the necessary conditions for producing quiescent radio emission. For example, the magnetized planets in our solar system (Mercury, Earth, Jupiter, Saturn, Uranus, Neptune) are "on", whereas the un-

magnetized solar system planets (Mars, Venus) are "off" (Khurana et al. 2004; Bolton et al. 2004; Girard et al. 2016; Mauk & Fox 2010; Kellermann 1970; Basharinov et al. 1974; Ganushkina et al. 2011). Similarly, deep observations of the nearest brown dwarf binary system Luhman 16AB (2.02±0.15 pc, Luhman 2013) and the Y dwarf WISE J085510.83071442.5 (2.23±0.16 pc, Tinney et al. 2014) rule out radio emission down to $[L_\nu] \leq 11.0$ and ≤ 11.2 erg s^{-1} Hz^{-1}, respectively, at 4σ significance (Osten et al. 2015; Kao et al. 2019).

Assuming that ultracool dwarfs emit only within the bounds $[L_{\nu,\mathrm{single}}] \in [11.7, 13.9]$ erg s^{-1} Hz^{-1} captures the observed range of detected ultracool dwarf quiescent radio luminosities. However, the existing set of detected objects may not fully capture the faint end of the ultracool dwarf luminosity distribution. Thus, we also include calculations for a hypothetical $\mathcal{P}(L_{\nu,\mathrm{single}})$ with $[L_{\nu,\mathrm{single}}] \in [9.8, 13.9]$ erg s^{-1} Hz^{-1}. Existing quiescent radio luminosities span 1.9 dex, and the revised lower limit reflects an additional 1.9 dex.

3.5. Applying the framework

Kao & Shkolnik (submitted) showed that L dwarfs may have a suppressed radio occurrence rate compared to M and T/Y dwarfs. We control for a possible dependence on spectral type by randomly drawing single-object systems without replacement to match the M, L, and T dwarf distribution of the individual components in the binary sample. The number of T dwarf systems available to draw from limits the sizes of our drawn samples to 112 objects. We account for different possible combinations of single-object systems by repeating this procedure 1000 times and calculating the probability density distribution of the occurrence rate for each trial.

We then take the mean distribution for single objects $\mathcal{P}(\theta_{\mathrm{single}})$ and transform it to a predicted distribution for binaries $\mathcal{P}(\theta_{\mathrm{predict}})$ by ensuring that

$$\int_{\theta_{\mathrm{single},1}}^{\theta_{\mathrm{single},2}} \mathcal{P}(\theta_{\mathrm{single}})d\theta_{\mathrm{single}} = \int_{\theta_{\mathrm{predict},1}}^{\theta_{\mathrm{predict},2}} \mathcal{P}(\theta_{\mathrm{predict}})d\theta_{\mathrm{predict}} \quad ,$$

where $\theta_{\mathrm{predict}} = 1 - (1 - \theta_{\mathrm{single}})^2$ (Eq. 9). We compare $\mathcal{P}(\theta_{\mathrm{predicted}})$ to the actual calculated binary radio occurrence rate distribution $\mathcal{P}(\theta_{\mathrm{binary}})$ in Figure 10.

Finally, we also calculate the probability density distribution for differences in occurrence rates $\Delta\theta$ between predicted and actual binary systems, where

$$\mathcal{P}(\Delta\theta) = \int_{-1}^{1} \mathcal{P}(\theta_{\mathrm{predict}})\mathcal{P}(\theta_{\mathrm{binary}} = \theta_{\mathrm{predict}} + \Delta\theta)\, d\theta_{\mathrm{predict}} \quad . \tag{10}$$

We can then calculate the probability that the binary radio occurrence rate exceeds the predicted occurrence rate by integrating

$$\mathbb{P}(\theta_{\mathrm{binary}} > \theta_{\mathrm{predict}}) = \int_0^1 \mathcal{P}(\Delta\theta)\, d\Delta\theta \quad . \tag{11}$$

3.6. Results: Occurrence rate of binary systems compared to predictions from single objects

In Figure 10, we show that binary ultracool dwarf systems have an elevated radio occurrence rate compared to the rate predicted from their single counterparts. This figure uses the full set of objects that have been observed at radio frequencies and assumes that $[L_{\nu,\mathrm{single}}] \in [11.7, 13.9]$ erg s^{-1} Hz^{-1}.

We find that the quiescent occurrence rate for the binary sample is $58^{+10}_{-11}\%$. For comparison, the predicted binary occurrence rate from single-object systems with the same spectral type distribution as our binary systems is $22^{+8}_{-7}\%$. Quoted uncertainties correspond to 68.3% credible intervals.

Additionally, we find that the radio occurrence rate of binaries exceeds the predicted rate from single objects with probability $\mathbb{P}(\theta_{\mathrm{binary}} > \theta_{\mathrm{predict}}) = 100\%$. We conclusively rule out the null hypothesis and further explore implications for the observed binary enhancement of radio occurrence rates in §4.

We find that binarity may enhance the ultracool dwarf quiescent radio occurrence rate even when we exclude objects from Kao et al. (2016). This targeted study selected objects with likely markers of auroral magnetic activity at other wavelengths such as Hα emission and infrared variability. These selection criteria resulted in a very high detection rate (80%) compared to the 5–10% detection rate in the literature (e.g. Route & Wolszczan 2016b; Richey-Yowell et al. accepted) that is consistent with that of volume-limited surveys (Antonova et al. 2013; Lynch et al. 2016, e.g.). Recently, Richey-Yowell et al. (accepted) showed that infrared photometric variability at 0.5–4 μm does not trace quiescent radio emission, but they reaffirm an earlier finding by Pineda et al. (2017) that Hα emission is correlated with the quiescent radio emission of ultracool dwarfs that have detected radio aurorae. Excluding these objects removes any obvious bias for magnetic activity in our samples. With the exception of the Kao et al. (2016) study, other survey attempts to introduce a positive detection bias have not yielded detection rates that are distinct from volume-limited studies (e.g. Richey-Yowell et al. accepted). Similarly, attempts to target individual objects that may be promising have yielded mixed results (e.g. Audard et al. 2005; Pineda & Hallinan 2018). We therefore elect to include all remaining available data to allow the hypothetical effects of these various selection attempts to average out.
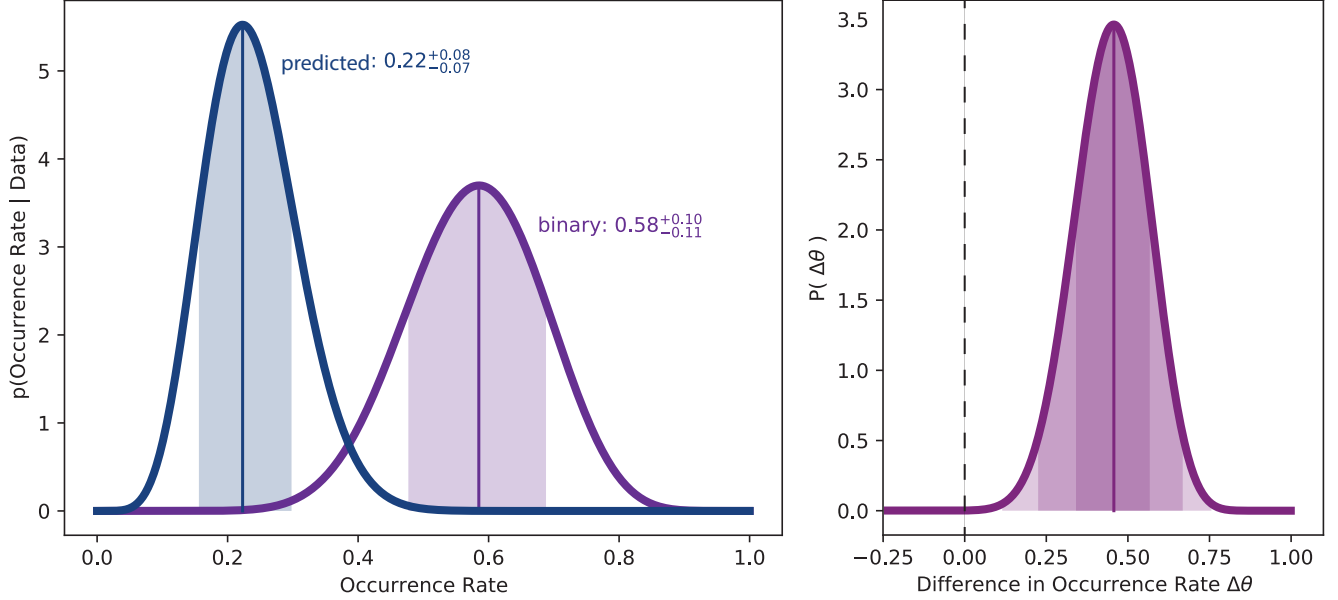
Figure 10. Calculations comparing binary to single-object systems using the full set of data available in the literature and assuming a uniform luminosity prior between $L_{\nu,\text{single}} \in [11.7, 13.9]$.
— Left: Occurrence rate distributions of quiescent radio emission in ultracool dwarf binaries (purple) and the predicted occurrence rate distribution for binaries from single objects, where $\theta_{\text{predicted}} = 1 - (1 - \theta_{\text{single}})^2$ (teal). Shaded regions correspond to the 68.3% credible intervals. Individual components in binary systems are more likely to emit radio emission than their single counterparts. — Right: Probability density distribution for the difference in occurrence rates $\Delta\theta = \theta_{\text{binary}} - \theta_{\text{predict}}$ between binaries and predictions from single objects. Shaded regions correspond to 68.3%, 95.5% and 99.7% credible intervals. Existing data rule out the null hypothesis that binarity does not affect quiescent radio occurrence rates.

For both datasets, we repeat this calculation for four luminosity distribution cases. We summarize these calculations in Table 6. In all cases, binary ultracool dwarfs have an elevated quiescent radio occurrence rate.

4. DISCUSSION

Comparing binary versus single-object systems gives strong evidence that binarity may enhance the quiescent radio activity of ultracool dwarfs. One possible contributor to the high binary occurrence rate may be that some of the included binary systems are in fact unresolved triples. With higher multiplicity, a greater fraction of combinations of radio-bright individual components can result in an unresolved system appearing radio-bright as a whole. However, ultracool dwarf triple systems are very rare (Bardalez Gagliuffi et al. 2014), and we have excluded all targets that have evidence of higher-order multiplicity.

An immediate implication of our results is that binaries are excellent targets for radio studies that aim to increase the number of known radio-bright ultracool dwarfs. Not only do they have an elevated radio occurrence rate compared to single objects, but they are also more luminous. As a result, binary systems at farther distances than single objects may be detectable, increasing the number

of observationally accessible systems. For instance, our targets 2MASS J21402931+1625183 and LP 415-20 are the most distant radio-bright ultracool dwarfs that have been detected to date, with distances of 33.1 ± 0.5 and 39.6884 ± 0.8060 pc, respectively. Before this work, the most distant radio-bright ultracool dwarf system was the binary 2MASS J09522188-1924319 (29.0 ± 0.13 pc) (McLean et al. 2012; Gaia Collaboration 2018). For comparison, the most distant detected single object is the L8.5 dwarf 2MASS J10430758+2225236 (Kao et al. 2016, 2018) at 16.4 ± 0.2pc (Schmidt et al. 2010).

The radio occurrence rates that we report are specifically for non-flaring radio emission. Since the quiescent emission that we focus on does not directly trace flares, our finding that binarity enhances the ultracool dwarf quiescent radio occurrence rate raises interesting questions about the plasma source for this emission.

A binary enhancement effect suggests that volcanic activity from satellites may not be the dominant source of magnetospheric plasma emission for ultracool dwarfs. Planet occurrence rates are suppressed for close-in binary stellar systems compared to wide-separation binaries and single-star systems (Moe & Kratter 2019). Theory suggests that this suppression occurs because binaries can truncate the mass and radius of the circumprimary

Table 6. Calculated occurrence rates

Dataset	Sample size (binary, single)	$\mathcal{P}(L_{\nu,\text{single}})$ $e = 1$	$L_{\min}, L_{\max}$ $e = 1$	θ_{binary}	θ_{predict}	$\mathbb{P}(\theta_{\text{binary}} > \theta_{\text{predict}})$
Literature	28, 112	Uniform	11.7–13.6	$0.58^{+0.10}_{-0.11}$	$0.22^{+0.08}_{-0.07}$	100%
Literature	28, 112	Uniform	9.8–13.6	$0.59^{+0.10}_{-0.11}$	$0.23^{+0.08}_{-0.07}$	100%
Literature	28, 112	KM	11.7–13.6	$0.67^{+0.11}_{-0.12}$	$0.27^{+0.09}_{-0.08}$	100%
Literature	28, 112	KM	9.8–13.6	$0.68^{+0.11}_{-0.12}$	$0.28^{+0.09}_{-0.08}$	100%
no K16[a]	27, 54	Uniform	11.7–13.6	$0.56^{+0.11}_{-0.11}$	$0.16^{+0.12}_{-0.09}$	100%
no K16[a]	27, 54	Uniform	9.8–13.6	$0.57^{+0.11}_{-0.11}$	$0.16^{+0.12}_{-0.09}$	100%
no K16[a]	27, 54	KM	11.7–13.6	$0.64^{+0.11}_{-0.12}$	$0.20^{+0.14}_{-0.11}$	100%
no K16[a]	27, 54	KM	9.8–13.6	$0.65^{+0.11}_{-0.12}$	$0.20^{+0.14}_{-0.11}$	100%

NOTE—For the single sample, single objects were randomly drawn from a samples of 82 ultracool M dwarfs, 74 L dwarfs, and 23 T/Y dwarfs to match the spectral type distribution of the individual components in the binary sample. Listed values are calculated from the mean distribution of 1000 trials. Reported uncertainties correspond to 68.3% credible intervals.

[a] Excluding observations from Kao et al. (2016, 2018) to reduce possible bias from their selection effects.

disk, increase disk turbulence, and/or clear out disk material on timescales faster than planet formation (e.g., Artymowicz & Lubow 1994; Haghighipour & Raymond 2007; Rafikov & Silsbee 2015). Like stars, ultracool dwarfs are known to host planets (e.g. the TRAPPIST-1 system, Gillon et al. 2017) and theory predicts multiple rocky planets around brown dwarfs (He et al. 2017). Thus, similar mechanisms may suppress planet formation around close-in brown dwarf binaries. In this scenario, we would also expect a suppressed quiescent radio occurrence rate if volcanic satellites are a key electron source. We emphasize, however, that our results do not rule out this mechanism. Instead, our results suggest that some other mechanism may on average outweigh the contribution of volcanic activity from satellites.

We additionally rule out excess flaring induced by magnetic interactions (e.g. Morgan et al. 2012; Lanza 2012). The smallest separation binaries in our sample (∼ 0.6 AU) rule out significant magnetospheric interactions. The strongest ultracool dwarf dipole fields (∼5 kG Kao et al. 2018) will decay by $1/r^3$ to $\lesssim$ 20 nG at the half-way point between binary components, which is less than ISM field strengths (Sofue et al. 2019).

One possibility may be that flaring activity provides a significant source of plasma for ultracool dwarf quiescent radio emission. For example, though no flares on T dwarfs have been detected yet, recent studies demonstrate that flares can occur on objects that are at least as late as L5 (Paudel et al. 2018a; Jackman et al. 2019; Paudel et al. 2020). If flaring activity seeds the magnetospheric plasma of ultracool dwarfs, then ultracool dwarf binaries may experience significant rotation-enhanced flaring. As noted in our introduction, tidal spin-up may enhance the rotation rates of stars and thus the magnetic activity of the stellar binary population (Zahn 1977; Morgan et al. 2016). Similar phenomena may occur for ultracool dwarfs. Alternatively, higher binary rotation rotation rates can result from shorter disk dissipation timescales in binary systems (Scholz et al. 2018).

However, existing studies suggest that flare activity may not correlate with radio activity. A study of flare frequency rates spanning M6–L0 spectral types suggests that flare frequencies decrease with later spectral types (Paudel et al. 2018a). Similarly, activity strengths of the chromospheric activity marker Hα decrease with later spectral types (Schmidt et al. 2015; Pineda et al. 2017). If flares indeed correlate with radio emission, we expect the latest type ultracool dwarfs to similarly exhibit a lower radio occurrence rate when all other factors are equal. Intriguingly, a comparison of quiescent radio occurrence rates between M, L and T/Y dwarfs tentatively demonstrates that while L dwarfs may have a lower radio occurrence rate than M dwarfs, T/Y dwarfs may not have a lower rate than L dwarfs (Kao & Shkolnik submitted). These findings tentatively suggest that flaring activity may not significantly contribute to the plasma reservoir that quiescent radio emission traces. While Kao & Shkolnik (submitted) do not control for other possible confounding factors such as age or rotation rate, their findings support evidence that radio ultracool dwarfs exhibit Hα activity that is distinct from flare activity (Pineda et al. 2017; Richey-Yowell et al. accepted).

Gaining further insight into flare contributions to the plasma reservoir traced by ultracool dwarf quiescent

radio emission will require studies that (1) examine how rotation rates correlate with ultracool dwarf flare rates and (2) compare the quiescent radio occurrence rate for flaring versus non-flaring ultracool dwarfs. If such studies find a higher occurrence rate of quiescent radio emission in flaring versus non-flaring objects, this may imply that flares provide a significant source of plasma in the magnetospheres of ultracool dwarfs.

This work has focused on comparing binary to single-object systems to study the underlying physical conditions powering ultracool dwarf radio emission. However, we also note that the radio observations presented here and the growing population of known radio-bright ultracool dwarf binaries will also be valuable benchmarks for calibrating magnetic models in the substellar mass regime. For instance, Mullan & MacDonald (2010) found that non-magnetic models cannot replicate both the observed luminosity and $T_{\rm eff}$ of GJ 564 BC. The addition of a strong internal magnetic field corresponding to a $\gtrsim$400 G surface field strength impedes the onset of convection and helps resolve this issue. If follow-up observations confirm that the tentative pulse that we observe from GJ 564 BC is indeed auroral in nature, the surface averaged magnetic field may be at least as strong as $\geq$1.3 kG (Kao et al. 2016).

Additional detections and confirmations of the circularly polarized auroral pulses that usually coexist with ultracool dwarf quiescent radio emission (e.g., Berger et al. 2001; Hallinan et al. 2007, 2008; Williams & Berger 2015; Kao et al. 2016, 2018) will yield more direct tests to calibrate such magnetism-dependent models.

5. CONCLUSIONS

We present the first detailed statistical comparison of non-flaring quiescent radio emission in ultracool dwarf binary systems compared to their single-object counterparts. Prior to this work, detection rate studies did not account for possible effects of binarity.

To supplement existing observations in the literature, we present new radio observations and detections of quiescent radio emission from three binary systems that were previously not known to be radio emitters. Our detections of 2MASS J21402931+1625183 and LP 415-20 represent the farthest known radio-bright ultracool dwarfs. We also tentatively detect a highly circularly polarized pulse at 4–6 GHz that may indicate aurorae from GJ 564 BC. These three new detections increase the number of known radio ultracool dwarf systems to 24.

We compile all published radio observations of binary ultracool dwarfs and compare the radio luminosities of binary systems to single objects. We show that although binarity appears to enhance the quiescent radio luminosities of detected ultracool dwarf binary systems relative to single objects, controlling for spectral types may account for this observed phenomenon.

Finally, we show how to apply a generalized analytical Bayesian framework for calculating the occurrence rate of steady emission in astrophysical populations introduced by Kao & Shkolnik (submitted) to comparisons between binary versus single-object systems in a rigorous and self-consistent manner. We then compare the quiescent radio occurrence rate of ultracool dwarf binary systems to single objects with a similar spectral type distribution as for our binary sample. We show that binarity enhances the the quiescent radio occurrence rate in ultracool dwarfs compared to their single counterparts.

REFERENCES

Antonova, A., Doyle, J. G., Hallinan, G., Golden, A., & Koen, C. 2007, A&A, 472, 257, doi: 10.1051/0004-6361:20077231

Antonova, A., Hallinan, G., Doyle, J. G., et al. 2013, A&A, 549, A131, doi: 10.1051/0004-6361/201118583

Artymowicz, P., & Lubow, S. H. 1994, ApJ, 421, 651, doi: 10.1086/173679

Audard, M., Brown, A., Briggs, K. R., et al. 2005, ApJL, 625, L63, doi: 10.1086/430881

Bardalez Gagliuffi, D. C., Gelino, C. R., & Burgasser, A. J. 2015, AJ, 150, 163, doi: 10.1088/0004-6256/150/5/163

Bardalez Gagliuffi, D. C., Burgasser, A. J., Gelino, C. R., et al. 2014, ApJ, 794, 143, doi: 10.1088/0004-637X/794/2/143

Basharinov, A. E., Gurvich, A. S., & Egorov, S. T. 1974, Moscow Izdatel Nauka

Berger, E. 2002, ApJ, 572, 503, doi: 10.1086/340301

—. 2006, ApJ, 648, 629, doi: 10.1086/505787

Berger, E., Ball, S., Becker, K. M., et al. 2001, Nature, 410, 338

Berger, E., Rutledge, R. E., Reid, I. N., et al. 2005, ApJ, 627, 960, doi: 10.1086/430343

Berger, E., Basri, G., Gizis, J. E., et al. 2008a, ApJ, 676, 1307, doi: 10.1086/529131

Berger, E., Gizis, J. E., Giampapa, M. S., et al. 2008b, ApJ, 673, 1080, doi: 10.1086/524769

Berger, E., Rutledge, R. E., Phan-Bao, N., et al. 2009, ApJ, 695, 310, doi: 10.1088/0004-637X/695/1/310

Blunt, S., Nielsen, E. L., De Rosa, R. J., et al. 2017, AJ, 153, 229, doi: 10.3847/1538-3881/aa6930

Bolton, S. J., Thorne, R. M., Bourdarie, S., de Pater, I., & Mauk, B. 2004, Jupiter's inner radiation belts, ed. F. Bagenal, T. E. Dowling, & W. B. McKinnon, 671–688

Bouy, H., Brandner, W., Martín, E. L., et al. 2003, AJ, 126, 1526, doi: 10.1086/377343

Bouy, H., Martín, E. L., Brandner, W., & Bouvier, J. 2005, AJ, 129, 511, doi: 10.1086/426559

Bouy, H., Duchêne, G., Köhler, R., et al. 2004, A&A, 423, 341, doi: 10.1051/0004-6361:20040551

Brandt, T. D., & Huang, C. X. 2015, ApJ, 807, 58, doi: 10.1088/0004-637X/807/1/58

Burgasser, A. J., Cruz, K. L., Cushing, M., et al. 2010, ApJ, 710, 1142, doi: 10.1088/0004-637X/710/2/1142

Burgasser, A. J., Kirkpatrick, J. D., & Lowrance, P. J. 2005, AJ, 129, 2849, doi: 10.1086/430218

Burgasser, A. J., & McElwain, M. W. 2006, AJ, 131, 1007, doi: 10.1086/499042

Burgasser, A. J., Melis, C., Todd, J., et al. 2015a, AJ, 150, 180, doi: 10.1088/0004-6256/150/6/180

Burgasser, A. J., Melis, C., Zauderer, B. A., & Berger, E. 2013a, ApJL, 762, L3, doi: 10.1088/2041-8205/762/1/L3

Burgasser, A. J., & Putman, M. E. 2005, ApJ, 626, 486, doi: 10.1086/429788

Burgasser, A. J., Sheppard, S. S., & Luhman, K. L. 2013b, ApJ, 772, 129, doi: 10.1088/0004-637X/772/2/129

Burgasser, A. J., Sitarski, B. N., Gelino, C. R., Logsdon, S. E., & Perrin, M. D. 2011a, ApJ, 739, 49, doi: 10.1088/0004-637X/739/1/49

Burgasser, A. J., Cushing, M. C., Kirkpatrick, J. D., et al. 2011b, ApJ, 735, 116, doi: 10.1088/0004-637X/735/2/116

Burgasser, A. J., Gillon, M., Melis, C., et al. 2015b, AJ, 149, 104, doi: 10.1088/0004-6256/149/3/104

Clarke, J. T., Grodent, D., Cowley, S. W. H., et al. 2004, Jupiter's aurora, ed. F. Bagenal, T. E. Dowling, & W. B. McKinnon, 639–670

Close, L. M., Siegler, N., Freed, M., & Biller, B. 2003, ApJ, 587, 407, doi: 10.1086/368177

Close, L. M., Siegler, N., Potter, D., Brand ner, W., & Liebert, J. 2002, ApJL, 567, L53, doi: 10.1086/339795

Deshpande, R., Martín, E. L., Montgomery, M. M., et al. 2012, AJ, 144, 99, doi: 10.1088/0004-6256/144/4/99

Dieterich, S. B., Henry, T. J., Jao, W.-C., et al. 2014, AJ, 147, 94, doi: 10.1088/0004-6256/147/5/94

Dieterich, S. B., Weinberger, A. J., Boss, A. P., et al. 2018, ApJ, 865, 28, doi: 10.3847/1538-4357/aadadc

Dupuy, T. J., Forbrich, J., Rizzuto, A., et al. 2016, ApJ, 827, 23, doi: 10.3847/0004-637X/827/1/23

Dupuy, T. J., & Liu, M. C. 2012, ApJS, 201, 19, doi: 10.1088/0067-0049/201/2/19

—. 2017, ApJS, 231, 15, doi: 10.3847/1538-4365/aa5e4c

Dupuy, T. J., Liu, M. C., & Ireland, M. J. 2009, ApJ, 692, 729, doi: 10.1088/0004-637X/692/1/729

Dupuy, T. J., Liu, M. C., Best, W. M. J., et al. 2019, AJ, 158, 174, doi: 10.3847/1538-3881/ab3cd1

Faherty, J. K., Burgasser, A. J., Cruz, K. L., et al. 2009, AJ, 137, 1, doi: 10.1088/0004-6256/137/1/1

Faherty, J. K., Burgasser, A. J., Walter, F. M., et al. 2012, ApJ, 752, 56, doi: 10.1088/0004-637X/752/1/56

Forbrich, J., Dupuy, T. J., Reid, M. J., et al. 2016, ApJ, 827, 22, doi: 10.3847/0004-637X/827/1/22

Forrest, W. J., Skrutskie, M. F., & Shure, M. 1988, ApJL, 330, L119, doi: 10.1086/185218

Gagné, J., Mamajek, E. E., Malo, L., et al. 2018, ApJ, 856, 23, doi: 10.3847/1538-4357/aaae09

Gaia Collaboration. 2018, VizieR Online Data Catalog, I/345

Ganushkina, N. Y., Dandouras, I., Shprits, Y. Y., & Cao, J. 2011, Journal of Geophysical Research (Space Physics), 116, A09234, doi: 10.1029/2010JA016376

Gauza, B., Béjar, V. J. S., Pérez-Garrido, A., et al. 2015, ApJ, 804, 96, doi: 10.1088/0004-637X/804/2/96

Gelino, C. R., Smart, R. L., Marocco, F., et al. 2014, AJ, 148, 6, doi: 10.1088/0004-6256/148/1/6

Gillon, M., Triaud, A. H. M. J., Demory, B.-O., et al. 2017, Nature, 542, 456, doi: 10.1038/nature21360

Girard, J. N., Zarka, P., Tasse, C., et al. 2016, A&A, 587, A3, doi: 10.1051/0004-6361/201527518

Gizis, J. E. 2002, ApJ, 575, 484, doi: 10.1086/341259

Gizis, J. E., Burgasser, A. J., Berger, E., et al. 2013, ApJ, 779, 172, doi: 10.1088/0004-637X/779/2/172

Gizis, J. E., Monet, D. G., Reid, I. N., et al. 2000, AJ, 120, 1085, doi: 10.1086/301456

Gizis, J. E., Williams, P. K. G., Burgasser, A. J., et al. 2016, AJ, 152, 123, doi: 10.3847/0004-6256/152/5/123

Golimowski, D. A., Henry, T. J., Krist, J. E., et al. 2004, AJ, 128, 1733, doi: 10.1086/423911

Guenther, E. W., & Wuchterl, G. 2003, A&A, 401, 677, doi: 10.1051/0004-6361:20030149

Guirado, J. C., Azulay, R., Gauza, B., et al. 2018, A&A, 610, A23, doi: 10.1051/0004-6361/201732130

Haghighipour, N., & Raymond, S. N. 2007, ApJ, 666, 436, doi: 10.1086/520501

Hallinan, G., Antonova, A., Doyle, J. G., et al. 2006, ApJ, 653, 690, doi: 10.1086/508678

—. 2008, ApJ, 684, 644, doi: 10.1086/590360

Hallinan, G., Bourke, S., Lane, C., et al. 2007, ApJL, 663, L25, doi: 10.1086/519790

Hallinan, G., Littlefair, S. P., Cotter, G., et al. 2015, Nature, 523, 568, doi: 10.1038/nature14619

Harding, L. K., Hallinan, G., Konopacky, Q. M., et al. 2013, A&A, 554, A113, doi: 10.1051/0004-6361/201220865

He, M. Y., Triaud, A. H. M. J., & Gillon, M. 2017, MNRAS, 464, 2687, doi: 10.1093/mnras/stw2391

Horne, R. B., Thorne, R. M., Glauert, S. A., et al. 2008, Nature Physics, 4, 301 EP . http://dx.doi.org/10.1038/nphys897

Hunter, J. D. 2007, Computing in Science and Engineering, 9, 90, doi: 10.1109/MCSE.2007.55

Jackman, J. A. G., Wheatley, P. J., Bayliss, D., et al. 2019, MNRAS, 485, L136, doi: 10.1093/mnrasl/slz039

Jones, E., Oliphant, T., Peterson, P., et al. 2001, SciPy: Open source scientific tools for Python. http://www.scipy.org/

Kao, M. M., Hallinan, G., & Pineda, J. S. 2019, MNRAS, 487, 1994, doi: 10.1093/mnras/stz1372

Kao, M. M., Hallinan, G., Pineda, J. S., et al. 2016, ApJ, 818, 24, doi: 10.3847/0004-637X/818/1/24

Kao, M. M., Hallinan, G., Pineda, J. S., Stevenson, D., & Burgasser, A. 2018, ApJS, 237, 25, doi: 10.3847/1538-4365/aac2d5

Kao, M. M., & Shkolnik , E. submitted, In prep.

Kaplan, E. L., & Meier, P. 1958, Journal of the American Statistical Association, 53, 457

Kellermann, K. I. 1970, Radio Science, 5, 487, doi: 10.1029/RS005i002p00487

Khurana, K. K., Kivelson, M. G., Vasyliunas, V. M., et al. 2004, The configuration of Jupiter's magnetosphere, ed. F. Bagenal, T. E. Dowling, & W. B. McKinnon, 593–616

Kirkpatrick, J. D., Reid, I. N., Liebert, J., et al. 2000, AJ, 120, 447, doi: 10.1086/301427

Koen, C. 2013, MNRAS, 428, 2824, doi: 10.1093/mnras/sts208

Köhler, R., Ratzka, T., & Leinert, C. 2012, A&A, 541, A29, doi: 10.1051/0004-6361/201118707

Konopacky, Q. M., Ghez, A. M., Barman, T. S., et al. 2010, ApJ, 711, 1087, doi: 10.1088/0004-637X/711/2/1087

Konopacky, Q. M., Ghez, A. M., Fabrycky, D. C., et al. 2012, ApJ, 750, 79, doi: 10.1088/0004-637X/750/1/79

Krishnamurthi, A., Leto, G., & Linsky, J. L. 1999, AJ, 118, 1369, doi: 10.1086/301015

Lanza, A. F. 2012, A&A, 544, A23, doi: 10.1051/0004-6361/201219002

Lazorenko, P. F., & Sahlmann, J. 2018, A&A, 618, A111, doi: 10.1051/0004-6361/201833626

Lee, E. T., & Wang, J. W. 2003, Statistical methods for survival data analysis, 3rd edn., Wiley series in probability and statistics (New York: J. Wiley)

Leinert, C., Allard, F., Richichi, A., & Hauschildt, P. H. 2000, A&A, 353, 691

Liu, M. C., Dupuy, T. J., & Allers, K. N. 2016, ApJ, 833, 96, doi: 10.3847/1538-4357/833/1/96

Luhman, K. L. 2013, ApJL, 767, L1, doi: 10.1088/2041-8205/767/1/L1

Lynch, C., Murphy, T., Ravi, V., et al. 2016, MNRAS, 457, 1224, doi: 10.1093/mnras/stw050

Martin, E. C., Mace, G. N., McLean, I. S., et al. 2017, ApJ, 838, 73, doi: 10.3847/1538-4357/aa6338

Mauk, B. H., & Fox, N. J. 2010, Journal of Geophysical Research (Space Physics), 115, A12220, doi: 10.1029/2010JA015660

McCaughrean, M. J., Scholz, R. D., & Lodieu, N. 2002, A&A, 390, L27, doi: 10.1051/0004-6361:20020928

McElwain, M. W., & Burgasser, A. J. 2006, AJ, 132, 2074, doi: 10.1086/508199

McLean, M., Berger, E., Irwin, J., Forbrich, J., & Reiners, A. 2011, ApJ, 741, 27, doi: 10.1088/0004-637X/741/1/27

22

McLean, M., Berger, E., & Reiners, A. 2012, ApJ, 746, 23, doi: 10.1088/0004-637X/746/1/23

McMullin, J. P., Waters, B., Schiebel, D., Young, W., & Golap, K. 2007, Astronomical Society of the Pacific Conference Series, Vol. 376, CASA Architecture and Applications, ed. R. A. Shaw, F. Hill, & D. J. Bell, 127

Miles-Páez, P. A., Pallé, E., & Zapatero Osorio, M. R. 2017, MNRAS, 472, 2297, doi: 10.1093/mnras/stx2191

Moe, M., & Kratter, K. M. 2019, arXiv e-prints, arXiv:1912.01699. https://arxiv.org/abs/1912.01699

Morgan, D. P., West, A. A., & Becker, A. C. 2016, AJ, 151, 114, doi: 10.3847/0004-6256/151/5/114

Morgan, D. P., West, A. A., Garcés, A., et al. 2012, AJ, 144, 93, doi: 10.1088/0004-6256/144/4/93

Mullan, D. J., & MacDonald, J. 2010, ApJ, 713, 1249, doi: 10.1088/0004-637X/713/2/1249

Osten, R. A., Hawley, S. L., Bastian, T. S., & Reid, I. N. 2006, ApJ, 637, 518, doi: 10.1086/498345

Osten, R. A., & Jayawardhana, R. 2006, ApJL, 644, L67, doi: 10.1086/505328

Osten, R. A., Melis, C., Stelzer, B., et al. 2015, ApJL, 805, L3, doi: 10.1088/2041-8205/805/1/L3

Osten, R. A., Phan-Bao, N., Hawley, S. L., Reid, I. N., & Ojha, R. 2009, ApJ, 700, 1750, doi: 10.1088/0004-637X/700/2/1750

Paudel, R. R., Gizis, J. E., Mullan, D. J., et al. 2018a, ApJ, 858, 55, doi: 10.3847/1538-4357/aab8fe

—. 2018b, ApJ, 861, 76, doi: 10.3847/1538-4357/aac8e0

—. 2020, arXiv e-prints, arXiv:2004.10579. https://arxiv.org/abs/2004.10579

Perley, R. A., Chandler, C. J., Butler, B. J., & Wrobel, J. M. 2011, ApJL, 739, L1, doi: 10.1088/2041-8205/739/1/L1

Phan-Bao, N., Osten, R. A., Lim, J., Martín, E. L., & Ho, P. T. P. 2007, ApJ, 658, 553, doi: 10.1086/511061

Pineda, J. S., & Hallinan, G. 2018, ApJ, 866, 155, doi: 10.3847/1538-4357/aae078

Pineda, J. S., Hallinan, G., & Kao, M. M. 2017, ApJ, 846, 75, doi: 10.3847/1538-4357/aa8596

Pineda, J. S., Hallinan, G., Kirkpatrick, J. D., et al. 2016, ApJ, 826, 73, doi: 10.3847/0004-637X/826/1/73

Potter, D., Martín, E. L., Cushing, M. C., et al. 2002, ApJL, 567, L133, doi: 10.1086/339999

Price-Whelan, A. M., Sipócz, B. M., Günther, H. M., et al. 2018, AJ, 156, 123, doi: 10.3847/1538-3881/aabc4f

Rafikov, R. R., & Silsbee, K. 2015, ApJ, 798, 69, doi: 10.1088/0004-637X/798/2/69

Reid, I. N., Cruz, K. L., Kirkpatrick, J. D., et al. 2008, AJ, 136, 1290, doi: 10.1088/0004-6256/136/3/1290

Reid, I. N., Kirkpatrick, J. D., Liebert, J., et al. 2002, AJ, 124, 519, doi: 10.1086/340805

Richey-Yowell, T., Kao, M. M., Pineda, J. S., Shkolnik, E., & Hallinan, G. accepted, ApJ

Route, M., & Wolszczan, A. 2012, ApJL, 747, L22, doi: 10.1088/2041-8205/747/2/L22

—. 2016a, ApJL, 821, L21, doi: 10.3847/2041-8205/821/2/L21

—. 2016b, ApJ, 830, 85, doi: 10.3847/0004-637X/830/2/85

Sault, R. J., Oosterloo, T., Dulk, G. A., & Leblanc, Y. 1997, A&A, 324, 1190

Schmidt, S. J., Cruz, K. L., Bongiorno, B. J., Liebert, J., & Reid, I. N. 2007, AJ, 133, 2258, doi: 10.1086/512158

Schmidt, S. J., Hawley, S. L., West, A. A., et al. 2015, AJ, 149, 158, doi: 10.1088/0004-6256/149/5/158

Schmidt, S. J., West, A. A., Hawley, S. L., & Pineda, J. S. 2010, AJ, 139, 1808, doi: 10.1088/0004-6256/139/5/1808

Scholz, A., Moore, K., Jayawardhana, R., et al. 2018, ApJ, 859, 153, doi: 10.3847/1538-4357/aabfbe

Scholz, R. D. 2014, A&A, 561, A113, doi: 10.1051/0004-6361/201323015

Scholz, R. D., McCaughrean, M. J., Lodieu, N., & Kuhlbrodt, B. 2003, A&A, 398, L29, doi: 10.1051/0004-6361:20021847

Siegler, N., Close, L. M., Cruz, K. L., Martín, E. L., & Reid, I. N. 2005, ApJ, 621, 1023, doi: 10.1086/427743

Siegler, N., Close, L. M., Mamajek, E. E., & Freed, M. 2003, ApJ, 598, 1265, doi: 10.1086/378935

Smart, R. L., Tinney, C. G., Bucciarelli, B., et al. 2013, MNRAS, 433, 2054, doi: 10.1093/mnras/stt876

Sofue, Y., Nakanishi, H., & Ichiki, K. 2019, MNRAS, 485, 924, doi: 10.1093/mnras/stz407

Stone, J. M., Skemer, A. J., Kratter, K. M., et al. 2016, ApJL, 818, L12, doi: 10.3847/2041-8205/818/1/L12

Stumpf, M. B., Brandner, W., Bouy, H., Henning, T., & Hippler, S. 2010, A&A, 516, A37, doi: 10.1051/0004-6361/200913711

Tinney, C. G., Faherty, J. K., Kirkpatrick, J. D., et al. 2014, ApJ, 796, 39, doi: 10.1088/0004-637X/796/1/39

Treumann, R. A. 2006, A&A Rv, 13, 229, doi: 10.1007/s00159-006-0001-y

van der Walt, S., Colbert, S. C., & Varoquaux, G. 2011, Computing in Science and Engineering, 13, 22, doi: 10.1109/MCSE.2011.37

Villadsen, J., & Hallinan, G. 2019, ApJ, 871, 214, doi: 10.3847/1538-4357/aaf88e

Villadsen, J., Hallinan, G., Bourke, S., Güdel, M., & Rupen, M. 2014, ApJ, 788, 112, doi: 10.1088/0004-637X/788/2/112

Weinberger, A. J., Boss, A. P., Keiser, S. A., et al. 2016, AJ, 152, 24, doi: 10.3847/0004-6256/152/1/24

Williams, P. K. G., & Berger, E. 2015, ApJ, 808, 189,
doi: 10.1088/0004-637X/808/2/189

Williams, P. K. G., Berger, E., Irwin, J., Berta-Thompson,
Z. K., & Charbonneau, D. 2015a, ApJ, 799, 192,
doi: 10.1088/0004-637X/799/2/192

Williams, P. K. G., Berger, E., & Zauderer, B. A. 2013,
ApJL, 767, L30, doi: 10.1088/2041-8205/767/2/L30

Williams, P. K. G., Casewell, S. L., Stark, C. R., et al.
2015b, ApJ, 815, 64, doi: 10.1088/0004-637X/815/1/64

Williams, P. K. G., Cook, B. A., & Berger, E. 2014, ApJ,
785, 9, doi: 10.1088/0004-637X/785/1/9

Zahn, J. P. 1977, A&A, 500, 121

Zhang, Q., Hallinan, G., Brisken, W., Bourke, S., & Golden,
A. 2020, ApJ, 897, 11, doi: 10.3847/1538-4357/ab9177